Journal of Marine Research, 51, 1–52, 1993

Journal of
MARINE RESEARCH

Volume 51, Number 1

The North Atlantic circulation: Combining simplified dynamics with hydrographic data

by Philip S. Bogden,[1,2] Russ E. Davis[1] and Rick Salmon[1]

ABSTRACT

We estimate the time-averaged velocity field in the North Atlantic from observations of density, wind stress and bottom topography. The flow is assumed geostrophic, with prescribed Ekman pumping at the surface, and no normal component at the bottom. These data and dynamics determine velocity to within an arbitrary function of (Coriolis parameter)/(ocean depth), which we call the "dynamical free mode." The free mode is selected to minimize mixing of potential density at mid-depth. This tracer-conservation criterion serves as a relatively weak constraint on the calculation.

Estimates of vertical velocity are particularly sensitive to variations in the free mode and to errors in density. In contrast, horizontal velocities are relatively robust. Below the thermocline, we predict a strong O(1 cm/sec) westward flow across the entire North Atlantic, in a narrow range of latitude between 25N and 32N. This feature supports the qualitative (and controversial) conjecture by Wüst (1935) of flow along the "Mediterranean Salt Tongue." Along continental margins and at the Mid-Atlantic Ridge, predicted bottom velocity points along isobaths, with shallow water to the right. These flows agree with many long-term current measurements and with notions of the circulation based on tracer distributions.

The results conflict with previous oceanographic-inverse models, which predict mid-depth flows an order of magnitude smaller and often in opposite directions. These discrepancies may be attributable to our relatively strong enforcement of the bottom boundary condition. This involves the plausible, although tenuous, assertion that the flow "feels" only the large-scale features of the bottom topography. Our objective is to investigate the consequences of using this hypothesis to estimate the North Atlantic circulation.

1. Scripps Institution of Oceanography, La Jolla, California, 92093-0230, U.S.A.
2. Present Address: Department of Earth, Atmospheric and Planetary Sciences, Massachusetts Institute of Technology, Cambridge, Massachusetts, 02139, U.S.A.

1. Introduction

If the ocean's mass density field and surface Ekman-pumping velocity are assumed to be known from observations, and if the large-scale time-averaged velocity is assumed to be

(a) geostrophic,
(b) hydrostatic,
(c) incompressible and
(d) tangent to the ocean bottom,

then the three-dimensional velocity field is determined up to a scalar function, $F(f/h)$, of the Coriolis parameter f divided by the ocean depth h. The function $F(f/h)$, which can be regarded as the undertermined part of the pressure field p, is the homogeneous solution of a two-dimensional hyperbolic equation determined by the data and assumptions (a–d). The characteristics are lines of constant f/h. These well known facts are reviewed in Section 2. We call the assumptions (a–d) our *dynamics*, and the undetermined part of the velocity field corresponding to $F(f/h)$ the *dynamical free mode.*

In this paper, we investigate the consequences of combining wind, hydrographic and bottom-topography data, the dynamics (a–d) and additional criteria needed to determine $F(f/h)$, to produce estimates of the large-scale, time-averaged circulation in the North Atlantic. We find that plausible variations in $F(f/h)$ and errors in the data lead to large vertical velocities that require mid-depth cross-isopycnal flows more than an order of magnitude larger than typical Ekman-pumping velocities. While reasonable bounds can be placed on cross-isopycnal flow magnitudes, the vertical velocity field is not reliably predicted. In contrast, horizontal velocities are relatively robust. Two features of the predicted sub-thermocline flow field are of particular interest. The first is a strong $O(1$ cm/sec) westward flow across the North Atlantic at mid-depth. This flow lies in a narrow $\approx 10°$ range of latitude near 30N. The second robust feature is a tendency for bottom velocity to follow isobaths, at the Mid-Atlantic Ridge and along both eastern and western boundaries, with shallow water to the right.

The predictions depend on the quality of the data (as representative of the large-scale time-average), the validity of our dynamical assumptions (a–d), and the criteria used to determine the free mode. The most problematical element of the dynamics is the assumption (d) of no-normal-flow at the ocean bottom. This is because the bottom kinematic boundary condition

$$w_b = -\mathbf{u}_b \cdot \nabla h \tag{1}$$

applies to the *fully resolved* (i.e. spatially unsmoothed) time-averaged flow and topography. (Here, w and $\mathbf{u} = (u, v)$ are the vertical and horizontal velocity, and the subscript b indicates evaluation at the ocean bottom $z = -h(\mathbf{x})$.) By applying (1) to the large-scale (i.e. spatially smoothed) fields, we incur errors arising from the

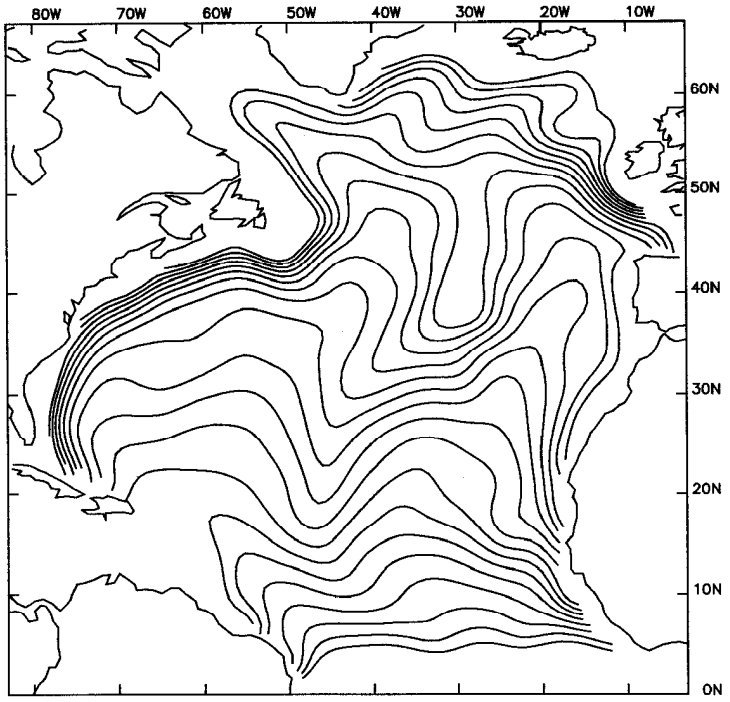

Figure 1. f/h contours. Varying contour interval keeps approximately uniform spacing between contours.

neglected contribution of small spatial scales to the right-hand side of (1). Scaling arguments (Bogden, 1991) suggest that these neglected contributions could be significant. Our objective is to investigate the assumption that they have no effect.

Removing small scales from the bathymetry affects the whole character of the hyperbolic problem. For fully resolved bathymetry, there are many closed contours of f/h. If, however, h is smooth (as we assume), then f/h contours traverse the entire ocean (Fig. 1). Free-mode selection, which amounts to the determination of $F(f/h)$, is then highly non-local along these contours; specifying $\mathbf{u} \times \nabla(f/h)$ at a single point $(\mathbf{x}, z)$ along an f/h contour determines velocity everywhere along that contour.

We select the free mode by demanding that our flow field be consistent with the average density equation

$$\mathbf{u} \cdot \nabla\theta + w\frac{\partial\theta}{\partial z} = \text{mixing} \tag{2}$$

with minimal "mixing," which corresponds to the Reynolds flux divergence. Here,

$$\theta \equiv \rho + \frac{g(z - z_0)}{c^2} \tag{3}$$

is an approximation to the potential density with reference depth z_0; ρ is density divided by 1 gm/cm^3 and c is sound speed at $z = z_0$. Mixing is clearly important in the ocean, but its importance relative to advection is unclear. Free-mode selection is based on a so-called "minimum-mixing" criterion that penalizes advective imbalance in (2), thereby minimizing cross-isopycnal flow.

Predictions of **u** are not sensitive to the exact details of the minimum-mixing criterion. This is because w is highly sensitive to free-mode variations, and mid-depth w's are so large that $|w\partial\theta/\partial z| \gg |\mathbf{u} \cdot \nabla\theta|$ in general. Therefore, the minimum-mixing criterion is nearly equivalent to a criterion of minimum $|w|$. The minimum-mixing criterion maintains reasonable bounds on cross-isopycnal flow, but details of the criterion cannot be manipulated to change the free mode significantly.

The velocity sensitivity to free-mode variations arises because the hyperbolic dynamics admit "front-like" features, i.e. arbitrarily large pressure gradients parallel to $\nabla(f/h)$. Front-like features appear, for example, in the solutions computed by Mellor *et al.* (1982) using a hyperbolic model, with $F(f/h)$ determined by a boundary condition on depth-integrated velocity. We find that the appearance of front-like features is linked to practical implementation of that boundary condition. Horizontal velocities in the front-like features align with f/h contours and have large subthermocline speeds of order 1 to 10 cm/sec. The associated vertical velocities require unreasonably large cross-isopycnal flows. For this reason, free-mode selection according to the minimum-mixing criterion dramatically reduces front-like features.

Even in the minimum-mixing solution, the residual mid-depth cross-isopycnal flows can be large compared to typical Ekman-pumping velocities. We investigate the possibility that the residual imbalances may result from small errors in the smoothed density field that make it dynamically incompatible with smoothed h. Explicit adjustments to ρ are designed to further reduce mixing through their impact on **u** and w. Adjustments of reasonable magnitude reduce the advective imbalance by as much as an order of magnitude in some regions, primarily by changing w. The optimized adjustments to ρ eliminate the front-like features, but leave large-scale features in **u** effectively unchanged. The analysis shows that w is particularly sensitive to density errors. In contrast, horizontal velocities are relatively robust.

The calculation predicts a relationship between the time-averaged flow and the "Mediterranean Salt Tongue," a prominent salinity feature near 1000 m depth associated with highly saline effluent from the Straits of Gibraltar. Several distinct flow schemes have been proposed to account for the salt tongue (e.g. Wüst, 1935; Worthington, 1976; Reid, 1978). Our predicted mid-depth westward flow along 30N supports the qualitative conjecture of Wüst (1935). Given the uncertainties of how the ocean mixes salinity, the only true test of the calculation is a comparison with direct measurements of time-averaged velocity. Those measurements from the region of strong westward-flow predictions support the calculation.

The subthermocline flows predicted here are typically an order of magnitude larger than in previous studies that determine velocity solely from geostrophic shear

and property-conservation constraints (e.g. Stommel and Schott, 1977; Olbers *et al.*, 1985; Hogg, 1987; Fukumori, 1991). In those studies the ocean bottom plays no role in estimating the flow and this appears to be the critical distinction. When the bottom boundary condition is not used, there is greater dynamical ambiguity (an arbitrary function of $\mathbf{x}$ can be added to $\mathbf{u}$) and the optimization procedures used to account for uncertain assumptions about property conservation and mixing evidently lead to minimizing deep flow. In the present study, the boundary condition (1) leads to the hyperbolic problem with the dynamical indeterminacy reduced to an arbitrary function of f/h. This reduced indeterminacy apparently forces more energetic mid-depth flow.

Two elements are critical to preserving the hyperbolic nature of the dynamics in a practical implementation with data. First, the fields of ρ and h must be continuous. Second, the dynamics must apply without misfit. Failure to satisfy both of these criteria accounts for the loss of hyperbolic structure in most models that incorporate the same dynamics and boundary conditions as used here (e.g. Wunsch, 1978; Provost and Salmon, 1986). These issues are discussed in Section 6. It is also worth noting that, despite the simplicity of the hyperbolic problem, numerical implementation requires care. After considerable experimentation, standard finite-difference methods were abandoned because the effects of truncation errors were intolerably large, and led to large spurious w's. Analogs of numerical diffusion also destroyed hyperbolicity. These and related problems (apparently also encountered by Mellor *et al.*, 1982) were eliminated by adopting a method based on dynamically self-consistent functional representations for all relevant fields and a numerical grid based on the f/h characteristics.

The paper is organized as follows. Section 2 reviews the hyperbolic dynamics, describes the data, and defines the dynamical free-mode and minimum-mixing criterion. Section 3 describes the numerical implementation and related issues. Section 4 presents the minimum-mixing circulation for the North Atlantic, and compares it to a solution using the usual eastern boundary condition. An analysis of the effects of density adjustments appears in Section 5. Robust flow predictions are presented in detail and compared to observations in Section 6. Relationships with previous studies are discussed in Section 7. Further discussion appears in Section 8.

2. The model

a. Data and hyperbolic dynamics. Outside thin boundary layers, the large-scale time-averaged circulation approximately satisfies

$$\begin{aligned} \mathbf{f} \times \mathbf{u} &= -\nabla p \\ 0 &= -\frac{\partial p}{\partial z} - g\rho \\ \nabla \cdot \mathbf{u} + \frac{\partial w}{\partial z} &= 0 \end{aligned} \tag{4}$$

where p and ρ are pressure and density, respectively, divided by 1 gm/cm^3. Here, density is prescribed using temperature and salinity from Levitus' (1982) climatological atlas. Knowledge of ρ combined with (4) determines $\partial \mathbf{u}/\partial z$, and specifies $\mathbf{u}$ up to an arbitrary function of horizontal position, $\mathbf{x}$. The velocity indeterminacy is equivalent to the statement that the horizontal geostrophic transport,

$$\mathbf{U}_g \equiv \int_{-h}^{0} \mathbf{u}\, dz = \hat{\mathbf{z}} \times \frac{1}{f} \int_{-h}^{0} \nabla p\, dz, \tag{5}$$

remains unknown, where $z = 0$ at the surface.

Boundary conditions at the surface and bottom reduce the velocity indeterminacy. The conditions are applied to the transport vorticity equation

$$\mathbf{U}_g \cdot \nabla f = f(w_0 - w_b) \tag{6}$$

where $w_0 \equiv w(z = 0)$ and $w_b \equiv w(z = -h)$. Eq. (6) follows from the horizontal divergence of (5). At the surface, Ekman pumping is prescribed from estimates of annual-average wind stress, $\boldsymbol{\tau}_0$ (Hellerman and Rosenstein, 1983). No-normal-flow through the free surface corresponds to

$$w_0 = w_e \equiv \hat{\mathbf{z}} \cdot \nabla \times (\boldsymbol{\tau}_0/f). \tag{7}$$

Using (1) and (7), Eq. (6) becomes

$$\mathbf{U}_g \cdot \nabla f = f(w_e + \mathbf{u}_b \cdot \nabla h). \tag{8}$$

All the physics of the hyperbolic problem are included in (8).

These physics are clearest in terms of the following transport components:

$$\begin{aligned} \mathbf{U}_b &\equiv h\mathbf{u}_b = \hat{\mathbf{z}} \times \frac{h}{f} (\nabla p)_b \\ \mathbf{U}_s &\equiv \int_{-h}^{0} (\mathbf{u} - \mathbf{u}_b)\, dz = \hat{\mathbf{z}} \times \frac{g}{f} \int_{-h}^{0} z\, \nabla \rho\, dz \\ \mathbf{U}_e &\equiv -\hat{\mathbf{z}} \times \boldsymbol{\tau}_0/f. \end{aligned} \tag{9}$$

$\mathbf{U}_b$ is an unknown horizontal transport associated with a depth-independent flow equal to the bottom velocity $\mathbf{u}_b$. The shear transport, $\mathbf{U}_s$, is the vertical integral of the geostrophic shear relative to $\mathbf{u}_b$, and is determined by ρ and h. $\mathbf{U}_e$ is the horizontal transport in the ageostrophic surface Ekman layer. Thus $\mathbf{U}_g = \mathbf{U}_b + \mathbf{U}_s$. The total horizontal transport, $\mathbf{U}$, includes $\mathbf{U}_e$,

$$\mathbf{U} \equiv \mathbf{U}_b + \mathbf{U}_s + \mathbf{U}_e \tag{10}$$

and $\nabla \cdot \mathbf{U} = 0$.

Using (9), (8) can be rewritten

$$\mathbf{U}_b \cdot \nabla(f/h) = \frac{1}{h}(-\mathbf{U}_s \cdot \nabla f + f w_e). \tag{11}$$

All the terms on the right can be computed from data. This shows that data and dynamics completely determine the component of $\mathbf{U}_b$ (and hence $\mathbf{u}$) parallel to $\nabla(f/h)$. An equivalent form for (8) is

$$\mathbf{U} \cdot \nabla(f/h) = f\,\mathbf{U}_s \cdot \nabla(1/h) + \nabla \cdot (f\,\mathbf{U}_e/h) \tag{12}$$

where again all the terms on the right are known from data. When h = constant, (12) reduces to the familiar Sverdrup relation.

Eq. (11) plus mass conservation form a hyperbolic system with characteristics f/h. This is made clear by writing (11) in terms of bottom pressure p_b,

$$\nabla p_b \times \nabla(f/h) = (f/h)^2[\nabla\gamma \times \nabla 1/f + \nabla \times (\boldsymbol{\tau}_0/f)] \tag{13}$$

where

$$\gamma \equiv \int_{-h}^{0} (p - p_b)\,dz = g\int_{-h}^{0} (z\rho)\,dz. \tag{14}$$

With h, ρ and $\boldsymbol{\tau}_0$ prescribed from data, the terms on the right of (13) are known and (with 4b) determine p up to the arbitrary function $F(f/h)$ that satisfies

$$\nabla F \times \nabla(f/h) = 0. \tag{15}$$

We refer to the arbitrary pressure field $F(f/h)$ as the dynamical free mode.

An alternative hyperbolic equation is obtained by writing (12) in terms of a transport stream-function, ψ,

$$\nabla\psi \times \nabla(f/h) = \nabla\gamma \times \nabla(1/h) + \nabla \times (\boldsymbol{\tau}_0/h) \tag{16}$$

where $\mathbf{U} \equiv \hat{\mathbf{z}} \times \nabla\psi$. This shows that ψ is determined by the data and dynamics up to an arbitrary function of f/h. The relationship between ψ and p_b is

$$\nabla\psi = \frac{1}{f}(\nabla\gamma + h\nabla p_b - \boldsymbol{\tau}_0) \tag{17}$$

b. Dynamical free mode. The dynamical free-mode velocity field has well-defined spatial structure. Free-mode horizontal velocity, $\mathbf{u}_F$, corresponds to an arbitrary depth-independent flow parallel to f/h isolines,

$$\mathbf{u}_F = \frac{F'}{f}\hat{\mathbf{z}} \times \nabla(f/h) \tag{18}$$

where $F' \equiv dF/d(f/h)$. The free-mode horizontal transport (using $\nabla \cdot (h\mathbf{u}_F) = 0$) is

$$\mathbf{U}_F \equiv h\mathbf{u}_F \equiv \hat{\mathbf{z}} \times \nabla\psi_F \tag{19}$$

where ψ_F and F are related by

$$d\psi_F = \frac{h}{f} dF. \tag{20}$$

The free-mode horizontal transport is everywhere parallel to f/h contours and corresponds to a constant mass flux between any two f/h contours.

Data and dynamics also determine w to within an arbitrary function proportional to F',

$$w_F = -\frac{zF'}{fh^2} \hat{\mathbf{z}} \cdot \nabla f \times \nabla h. \tag{21}$$

Note that w_F varies along f/h in proportion with the zonal gradient in bottom depth, $\partial h/\partial x$. When $\partial h/\partial x = 0$, $w_F = 0$, so that the vertical-velocity profile is independent of free-mode variations. In this case, w is completely determined by data and dynamics so that, for example,

$$w_b = \frac{1}{f}\frac{\partial h}{\partial y}(\hat{\mathbf{z}} \cdot \nabla\gamma \times \nabla 1/f + w_e)\left(\frac{\partial(h/f)}{\partial y}\right)^{-1} \quad \text{for} \quad \frac{\partial h}{\partial x} = 0. \tag{22}$$

An important ramification of this dependence of w_F on the local bathymetry is that w is most sensitive to variations in F where the zonal gradients in h are largest.

$\mathbf{U}_F$, $\mathbf{u}_F$ and w_F all vary in proportion to F', which is constant along f/h contours. Without the boundary conditions (1) and (7) the velocity is determined up to an unknown function of position $\mathbf{x}$. With boundary conditions, indeterminacy reduces to a function of the scalar f/h. Specifying $\mathbf{u} \times \nabla(f/h)$ (or w, if $z \neq 0$ and $\partial h/\partial x \neq 0$) at any point along an f/h contour determines F' and hence velocity everywhere along that contour.

A set of f/h contours for the North Atlantic, computed from smoothed bottom topography, is plotted in Figure 1. The contours traverse the North Atlantic with only one area of closed contours near 40N, 30W. This region, associated with a shallow portion of the Mid-Atlantic Ridge, will be referred to as the "shadow dome." Flow within the shadow dome is not modeled here since the data-dependent terms in (13) do not guarantee single-valued solutions when contours close. If rougher topography is used, f/h contains more smaller-scale closed-contour regions. The smoothing of h has eliminated the small-scale features.

c. Implications of spatial smoothing. Scaling arguments show that (8) is a reasonable approximation of the *time-averaged* dynamics. (Eqs. 11, 12, 13 and 16 are each

equivalent to 8.) Neglecting Reynolds stresses is probably the most severe assumption and is likely to be critical near the lateral boundaries. Away from lateral boundaries, however, observational estimates of the Reynolds stresses show that these terms are small relative to those retained (e.g. Bogden, 1991).

The most tenuous assumption made in this study is the application of (8) to the *spatially averaged* fields. In principle, smooth fields satisfy a correspondingly smoothed version of (8) that includes additional terms associated with unresolved scales. Consider, for example, a spatial smoothing operator $\{\cdot\}$ defined so that the time-averaged spatially resolved field of (say) $\mathbf{u}$ can be written $\mathbf{u} = \{\mathbf{u}\} + \hat{\mathbf{u}}$, where $\hat{\mathbf{u}}$ is the small-scale field. Clearly (1) applies to resolved fields of w_b, $\mathbf{u}_b$ and h, but the smooth version of (1) is

$$-\{w_b\} = \{\mathbf{u}_b \cdot \nabla h\} = \{\{\mathbf{u}_b\} \cdot \nabla\{h\}\} + \{\hat{\mathbf{u}}_b \cdot \nabla\{h\}\} + \{\{\mathbf{u}_b\} \cdot \nabla\hat{h}\} + \{\hat{\mathbf{u}}_b \cdot \nabla\hat{h}\}. \quad (23)$$

The fourth term on the right represents the average contribution from the product of unresolved scales. Since $\{\cdot\}$ represents an average over a finite area, $\{\{\mathbf{u}\}\} \neq \{\mathbf{u}\}$ and $\{\nabla h\} \neq \nabla\{h\}$ in general. Therefore, the second and third terms on the right of (23) cannot be neglected on the basis of averaging alone, as they would be in a Reynolds average. Scaling arguments indicate that the terms involving unresolved scales can be important. There is some evidence in time-averaged current measurements that the last term in (23) may be negligible. Fu *et al.* (1982), for example, find that time-averaged currents near the bottom tend to align with local small-scale features in the bathymetry, which implies $\hat{\mathbf{u}}_b \cdot \nabla\hat{h} \approx 0$. Any misalignment in the vectors could contribute dynamically large values of $\{w_b\}$. We acknowledge the uncertainty associated with the unresolved spatial scales and adopt the simple model

$$\{w_b\} = -\{\mathbf{u}_b\} \cdot \nabla\{h\} \quad (23)$$

as a working hypothesis. We likewise assume that (8) applies when all variables represent spatially smoothed fields. The best we can hope to do is test this hypothesis by comparing robust predictions with direct measurements of the large-scale time-averaged fields.

Whether the hypothesis (24) is correct or not, account must also be taken of the errors introduced into the *measured* smooth fields by differences in how ρ and h are smoothed, by sparse observations and, for ρ at least, by time variability. The smoothing of $h(\mathbf{x})$ is described by Bogden (1991), and Levitus (1982) describes smoothing of temperature and salinity from which ρ is calculated. Regardless of the error source, both ρ and h may be in error and the impact of this error must be assessed. If $\{\cdot\}$ denotes the true smooth fields, the available estimated fields are $\{\rho\} + \tilde{\rho}$ and $\{h\} + \tilde{h}$, where $\tilde{\rho}$ and $\tilde{h}$ are errors. These fields enter the dynamics (11) through $\{\mathbf{U}_s\}$, as defined in (9), which involves the integral

$$\int_{-\{h\}}^{0} z\nabla\{\rho\}\, dz. \quad (25)$$

When this integral is evaluated from the available fields $\{\rho\} + \tilde{\rho}$ and $\{h\} + \tilde{h}$, the error is

$$\int_{-\{h\}-\tilde{h}}^{-\{h\}} z\nabla\{\rho\}\, dz + \int_{-\{h\}}^{0} z\nabla\tilde{\rho}\, dz + \int_{-\{h\}-\tilde{h}}^{-\{h\}} z\nabla\tilde{\rho}\, dz. \tag{26}$$

Over most of the ocean it is likely that $|\nabla\tilde{\rho}| \ll |\nabla\{\rho\}|$ and $|\tilde{h}| \ll h$ so that the last term is smallest. In shallow water $|\tilde{h}|$ and $\{h\}$ may be comparable, in which case the first term will dominate. Over most of the domain, however, the water is deep and the relative error $|\tilde{h}/\{h\}|$ is much smaller than error $|\nabla\tilde{\rho}/\nabla\{\rho\}|$. Thus in most places the error is dominated by the second term in (26) and density errors are likely the more important.

d. Minimum-mixing criterion. Data and dynamics determine pressure up to the arbitrary function $F(f/h)$, the dynamical free mode. Recall that specifying $\mathbf{u} \times \nabla(f/h)$ at any point along an f/h contour eliminates the indeterminacy. Our criterion for free-mode selection is to minimize mixing in an approximation of the time-averaged density equation (2). The minimum-mixing solution is obtained by selecting the free mode that minimizes

$$B_0 = \int\int f^2\, |\mathbf{u} \cdot \nabla\theta + w\, \partial\theta/\partial z|^2\, d\mathbf{x}. \tag{27}$$

(The factor of f^2 compensates for a singularity in the geostrophic velocity at the equator.) In this study, B_0 is evaluated in the horizontal plane at 1000 m depth. This is deeper than the main thermocline in the North Atlantic, yet at a depth where strong signals in a variety of property distributions indicate that advection is important (see Section 6). Near lateral boundaries we suppose that mixing could be large. Therefore, unless otherwise specified, areas within roughly 500 km of the coasts are excluded from the evaluation of B_0.

Based on results presented in Section 4, the details of the minimum-mixing criterion are not critical in the analysis that follows. There it is shown that the calculation can produce front-like features with large vertical velocities. These features require unreasonably large cross-isopycnal flows. We use (27) as a weak constraint to bound the cross-isopycnal flows within a plausible range of values (see discussion in Sections 7 and 8). Thus (27) serves primarily to penalize the front-like features. Below the main thermocline the front-like features have simple vertical structure: $|w|$ increases nearly linearly in z to a maximum at the bottom while $|\mathbf{u}|$ remains relatively constant. Therefore, the results are insensitive to the depth at which the minimum-mixing criterion is applied. Further refinement of (27) would be justified were we to use tracer-conservation as a stronger constraint in the calculation. We do not investigate the limit in which cross-isopycnal mixing is negligible, however, nor do we attempt to model the residual advective imbalance.

3. Numerical method

This section presents the numerical formulation of the hyperbolic problem. In developing the method, we encountered problems with standard finite-difference methods. Related problems have apparently been encountered in previous studies using similar hyperbolic dynamics (e.g. Mellor *et al.*, 1982). This section begins by identifying the nature of the problems and then describes the numerical formulation used to overcome them.

Difficulties stem from the truncation errors inherent to finite-differences. Centered differences have second-order accuracy on a uniform grid. This means that if $h(\mathbf{x})$ is linear in $\mathbf{x}$, then a centered-difference estimate of ∇h^2 computed from gridded values of h^2 recovers the true value $2h\nabla h$. In contrast, a centered-difference estimate of ∇h^3 computed from gridded h^3 equals $(3h^2\nabla h + \epsilon)$, where $\epsilon \times \nabla h \neq 0$ in general. With a non-uniform grid, centered differences are only accurate to first order so that ∇h^2 computed from gridded h^2 has errors. In this study, a non-uniform grid was used to integrate the hyperbolic dynamics along f/h characteristics.

These comments are relevant in part because γ has a strong h-dependence and the right-hand side of (16) involves the product $\nabla\gamma \times \nabla h$. (If ρ = *constant* then γ varies as h^2, and if ρ = *constant* z then γ varies as h^3. Related finite-difference errors reduce, but do not disappear, by subtracting a horizontally averaged density profile from ρ before computing γ.) Mellor *et al.* (1982) attribute their computation of "noisy" ψ to errors in computing $\nabla\gamma \times \nabla h$. They address the problem by introducing the new variable $\chi \equiv \psi - \gamma/f$ so that (16) becomes

$$\nabla\chi \times \nabla(f/h) = -\frac{1}{f}\nabla(\gamma/h) \times \nabla f + \nabla \times (\tau_0/h). \tag{28}$$

Although the right-hand side still involves $\nabla\gamma$, it no longer involves the cross-product of generally parallel vectors. While the transformation leads to a "smoother" right-hand side, it simply defers the introduction of numerical error into the velocity computation. These errors have a particularly large impact on w. For example, in terms of ψ

$$w_b = (1/h)\hat{\mathbf{z}} \cdot (-\nabla\psi + (1/f)\nabla\gamma - \tau_0/f) \times \nabla h \tag{29}$$

involves the troublesome product $\nabla\gamma \times \nabla h$. In terms of χ,

$$w_b = (1/h)\hat{\mathbf{z}} \cdot (-\nabla\chi - \gamma\nabla(1/f) - \tau_0/f) \times \nabla h. \tag{30}$$

Although $\nabla\gamma$ does not appear explicitly in (30), the troublesome term involves $\nabla\chi$ because $\chi \sim \gamma$. Numerical errors that lead to spurious w_b arise when computing $\nabla\chi \times \nabla h$. The computational liability associated with differentiating γ (or χ) can be

reduced by computing $\nabla\gamma \times \nabla h$ from the identity

$$\nabla\gamma \times \nabla h = g \int_{-h}^{0} (\nabla\rho \times \nabla h)\, z\, dz. \tag{31}$$

Since ρ and h do not have a built-in non-linear functional relationship, discretizing the right-hand side of (31) is less susceptible to numerical error.

Finite-difference errors remain important regardless of mathematical formulation, however, because the hyperbolic dynamics admit arbitrarily large gradients in ψ or p parallel to $\nabla(f/h)$. As is demonstrated in Section 4, large gradients appear in the results depending on the choice of free mode. We found that errors in the finite-difference representation of these gradients accounted for large spurious w's.

Finite-difference inaccuracies are eliminated in this study by using a numerical scheme that exactly solves a closely related realizable physical model. Relevant fields are interpolated between grid points using physically self-consistent low-order polynomial representations. For example, ρ is linearly interpolated in z between standard levels defined by Levitus (1982). The physically self-consistent pressure field has quadratic z-dependence by the hydrostatic balance, $\partial p/\partial z = -g\rho$. In the horizontal, h, $1/f$ and τ_0 are selected to vary linearly in distance between grid points. However, p and ρ vary in linear proportion with the product $(h)(1/f)$, which makes p and ρ quadratic in $\mathbf{x}$. For reasons described below, this horizontal interpolation scheme preserves the hyperbolic structure of the dynamics. With these explicit polynomial representations, integration, differentiation and physical balances are exact; there are no numerical inaccuracies. The piecewise polynomials do not, of course, exactly represent the continuous fields but do represent an exactly self-consistent approximation. Adequate resolution in the grid is needed so that the numerical representation is realistic.

The algorithm for computing p is obtained by balancing the mass flux across the surfaces of contiguous cylindrical volumes extending from some arbitrary depth $z = -r(\mathbf{x})$ to the bottom at $z = -h(\mathbf{x})$. The volume integral of (4c) is

$$\iiint \frac{\partial w}{\partial z}\, dz\, d\mathbf{x} = -\iiint \nabla \cdot \mathbf{u}\, dz\, d\mathbf{x}. \tag{32}$$

Integrating vertically using (1) yields an equation for w_r, the vertical velocity through the surface $z = -r(\mathbf{x})$.

$$\iint w_r\, d\mathbf{x} = -\oint \hat{\mathbf{n}} \cdot \int \mathbf{u}\, dz\, ds - \iint \mathbf{u}_r \cdot \nabla r\, d\mathbf{x} \tag{33}$$

$\hat{\mathbf{n}}$ is an outward unit-normal, s is a coordinate along the perimeter increasing in the counter-clockwise sense and the subscript r denotes evaluation on the surface $z = -r$. In terms of p,

$$\iint w_r\, d\mathbf{x} = \oint 1/f \int (dp/ds)\, dz\, ds - \iint 1/f\, \hat{\mathbf{z}} \cdot \nabla p_r \times \nabla r\, d\mathbf{x}. \tag{34}$$

Using (4) and integration by parts yields

$$\int\int w_r \, d\mathbf{x} = -\oint p_b d(h/f) + \oint (r p_b - \int \eta \, dz) d\,(1/f) + \int\int \hat{\mathbf{z}} \cdot \nabla(1/f) \times p_r \nabla r \, d\mathbf{x} \qquad (35)$$

where

$$p(z) = p_b + \eta \qquad \text{and} \qquad \eta(z) \equiv -g\int_{-h}^{z} \rho \, dz'. \qquad (36)$$

Letting $r \to 0$ and setting $w_0 = w_e$ yields

$$\oint (\boldsymbol{\tau}_0/f) \cdot d\mathbf{s} = -\oint p_b \, d(h/f) - \oint \gamma d(1/f). \qquad (37)$$

Eq. (37) is the area-integral form of (13). The corresponding equation for p_r is

$$\oint p_r \, d(h/f) = -\oint \gamma d(1/f) - \oint (\boldsymbol{\tau}_0/f) \cdot d\mathbf{s} + \oint \eta_r \, d(h/f) \qquad \text{for } r = \text{constant}. \qquad (38)$$

Each of the contour integrals on the right is evaluated for elemental areas formed by integrating along the line segments that connect adjacent grid points. The operation uses prescribed values of ρ, $\boldsymbol{\tau}_0$, h and $1/f$ at each grid point (see Bogden, 1991).

Elemental areas are based on a horizontal non-overlapping triangular mesh. The triangular mesh is developed from f/h contours as in Figure 1. (A non-uniform contour interval maintains roughly constant spacing between contours.) Non-overlapping triangles (Fig. 2) are obtained by interconnecting the individual line segments lying on adjacent contours. Each triangle has two vertices with the same value of f/h and a third vertex on an adjacent f/h contour. The area devoid of triangles within the shadow dome is excluded from the analysis.

The fundamental grid element for evaluating (38) is a diamond formed by two triangles whose common segment lies on an f/h contour. Consider, for example, a subset of the grid comprised of three f/h contours in Figure 3. Four vertices of a typical element are numbered counterclockwise with vertices 1 and 3 lying on the same f/h contour. Apart from occasional simple triangles on the boundary of the computational domain, the entire numerical mesh can be constructed from these diamond-shaped elements. Since p_r varies linearly in h/f along the perimeter of the fundamental elements, i.e. along the dashed lines in Figure 3, the following contour integral is exact

$$\oint p_r \, d(h/f) = \tfrac{1}{2}\,(p_1 - p_3)([h/f\,]_2 - [h/f\,]_4). \qquad (39)$$

Notice that the right-hand-side of (39) involves the difference of p at triangle vertices lying on the same contour. With the left-hand-side of (39) evaluated from (38), these differences can be integrated along each contour, one at a time, to provide a value of pressure at each of the nodes making up the contour. Eq. (17) is integrated between triangle nodes to find the corresponding values of ψ.

This algorithm determines p and ψ up to an arbitrary constant on each contour.

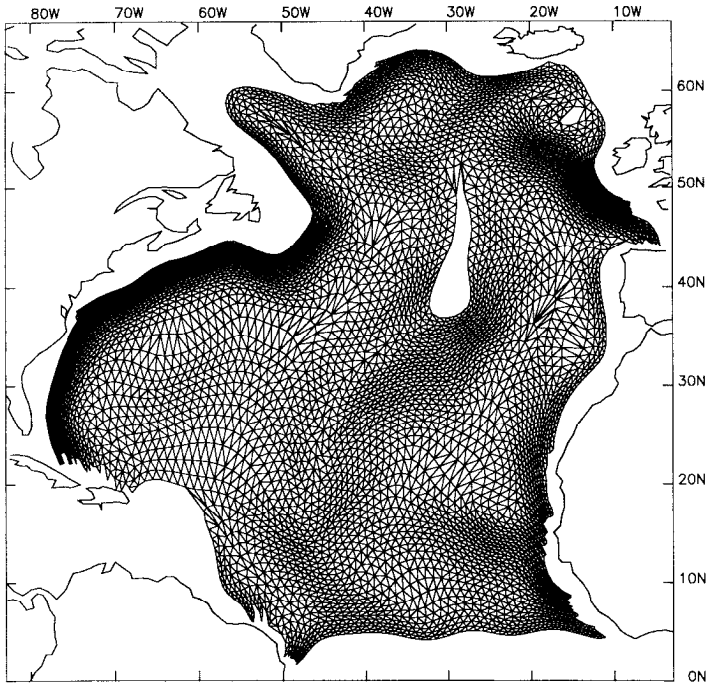

Figure 2. Numerical grid based on $72 f/h$ contours.

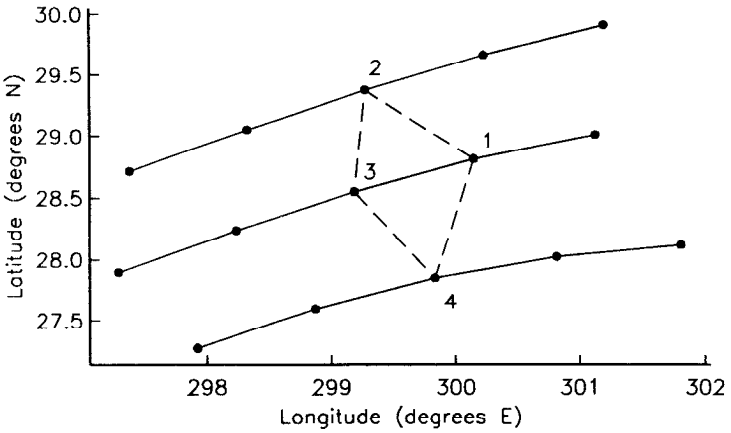

Figure 3. Portion of numerical grid. Solid lines connect grid points on f/h characteristics. Dashed lines connect grid points of a representative fundamental element.

This constant is the numerical analog of the dynamical free mode, $F(f/h)$. It is important to note that since F corresponds to a pressure, F varies linearly in h/f along the perimeter of elements. Consequently, the integral form of (15),

$$\oint F d(h/f) = \tfrac{1}{2}(F_1 - F_3)([h/f]_2 - [h/f]_4) = 0 \tag{40}$$

is also exact because $F_1 = F_3$.

Because the f/h contours define the numerical mesh, it is possible to preserve the numerical equivalent of hyperbolicity. In particular, adding a constant to p on a contour produces the same change all along that contour and none on its neighbors—this is the numerical free mode. Basing the finite-element grid on the f/h characteristics and choosing p_r and ρ to vary linearly in h/f is important to preserving the hyperbolic nature of the dynamics. Consider the consequences if p had been chosen to vary linearly in **x**. In that case, the right-hand side of (39) would include a small dependence on p_2 and p_4 due to the quadratic **x**-dependence of h/f. Adding a constant to the pressure on contours passing through points 2 or 4 then changes the right-hand side of (39), which means that free-mode variations would affect the numerical value of $\nabla p \times \nabla(h/f)$, violating the hyperbolic dynamics. By choosing p and ρ to vary linearly in h/f, arbitrarily large free-mode variations affect only the numerical equivalent of $\nabla p \cdot \nabla(h/f)$. Preserving the hyperbolic nature of the dynamics has the related benefit of simplifying the computation by allowing p to be integrated along characteristics.

4. Minimum-mixing solution

To demonstrate sensitivity to free-mode selection, the minimum-mixing solution is compared to an alternate solution that differs only with respect to the choice of free mode. The alternate criterion sets the free mode so that depth-integrated horizontal velocity normal to the eastern boundary is zero; we refer to this as the "ψ(east) = 0 boundary condition." Results in this section demonstrate that free-mode selection according to the ψ(east) = 0 condition leads to front-like features when applied with realistic topography.

a. Flat-bottomed models and the ψ(east) = 0 boundary condition. A common idealization in analytical models of the wind-driven circulation involves setting $h = constant$, so that $w_b = 0$ in (1). In this case, (8) reduces to

$$\mathbf{U} \cdot \nabla f = \hat{\mathbf{z}} \cdot \nabla \times \tau_0 \qquad \text{when } h = constant. \tag{41}$$

This is the classical Sverdrup relation (Sverdrup, 1947) in which τ_0 alone determines meridional transport. Eq. (41) is solved by integrating the associated hyperbolic equation for ψ along latitude lines. Typically, the dynamical free mode (here a

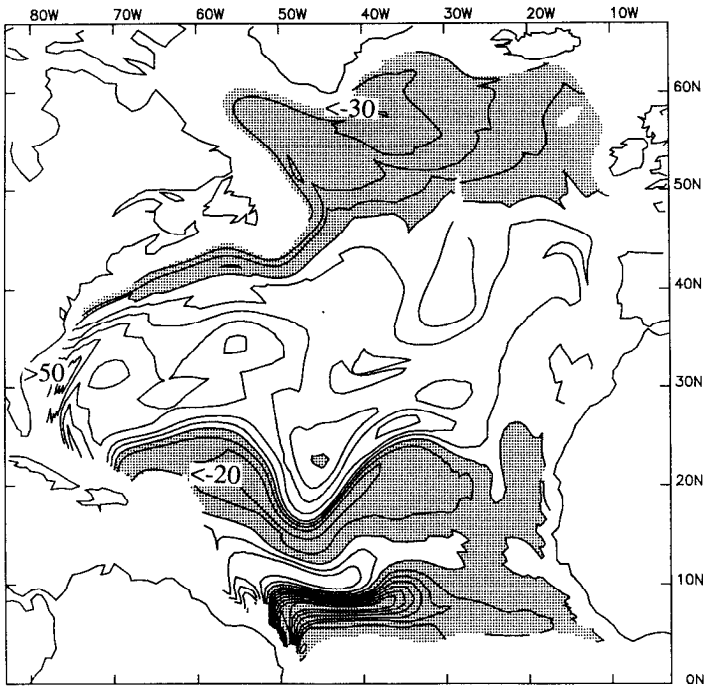

Figure 4. ψ for the ψ(east) = 0 solution. Contour interval: 10 Sverdrups. Negative values are shaded. (1 Sverdrup $\equiv 10^6 m^3/sec$.)

function of f) is chosen so that ψ is a constant on the eastern boundary—the ψ(east) = 0 boundary condition. ψ for the flat-bottom problem in the North Atlantic (see Bogden, 1991, Figure 3.1) contains well-known features: an anticyclonic subtropical circulation between 20N and 50N, and a sub-polar flow in the opposite sense north of 50N.

While ψ(east) = 0 assures no transport into the eastern boundary, the solution has approximately 30 Sverdrups (1 Sverdrup = $10^6 m^3/sec$) flowing into the western boundary between 15N and 30N, and a similar amount flowing out of the western boundary between 30N and 50N. This standard result is reasonable because higher-order dynamics lead to a western boundary current which closes the circulation. While plausible, the ψ(east) = 0 condition includes the tenuous assumption that any unresolved eastern-boundary dynamics have negligible influence on mid-ocean transport.

Additional subjectivity in applying the ψ(east) = 0 condition arises in the realistic case where $h \neq$ constant. Unless the lateral boundary is modeled as a vertical wall, as is the case when h = constant, unclosed f/h contours continue into shallow water at low latitudes. Eventually, the contours terminate on the beach at the equator where both f and h approach zero in the appropriate ratio. Clearly, higher-order ageo-

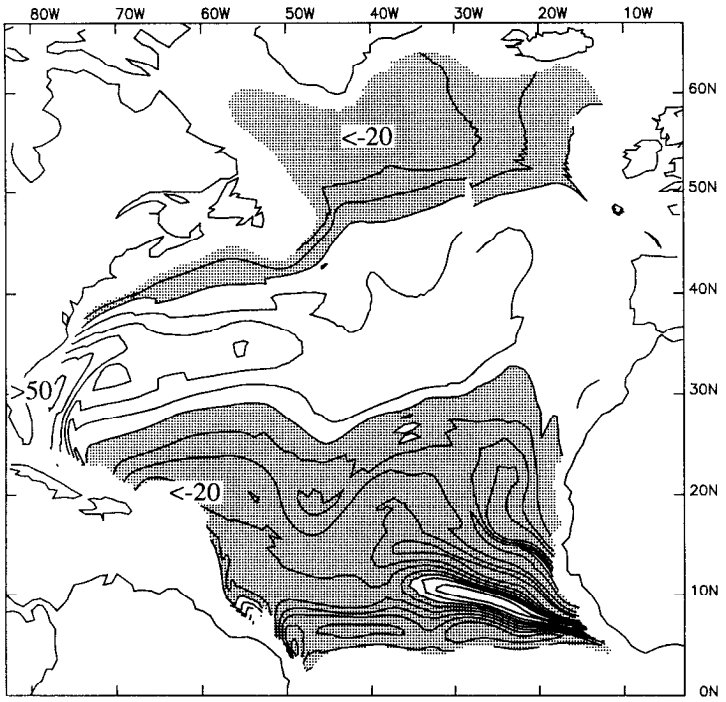

Figure 5. Minimum-mixing streamfunction ψ. Contour intervals as in Figure 4.

strophic dynamics come into play before this theoretical limit is reached. In the analysis below, the free mode is selected so that $\psi = 0$ at the eastern edge of the computational domain, which is arbitrarily chosen to be near the 1000 m isobath.

b. Realistic bathymetry: Minimum-mixing versus ψ(east) = 0. The transport streamfunction ψ for the problem with realistic bathymetry is presented in Figures 4 and 5. Both fields are solutions to the hyperbolic problem described in Section 2. They differ only in the choice of dynamical free mode, $F(f/h)$.

Large-scale features in the ψ(east) = 0 solution (Fig. 4) resemble the flat-bottom solution. These include the cyclonic circulation between 20N and 50N, and anticyclonic circulation north of 50N. There are many more large-gradient features in Figure 4, however. Two features are particularly noteworthy. The first is cyclonic flow around the shadow-dome, the closed f/h-contour region near 40N and 30W. The second is a large-amplitude front-like feature in the mid-ocean that runs along f/h contours near 20N.

The ψ(east) = 0 condition was used to estimate the North Atlantic circulation by Mellor *et al.* (1982). Although they used the hyperbolic dynamics in Section 2, they used rougher bottom topography and smoothed their result to obtain a solution in the numerous closed-contour regions. (No smoothing of the solutions is used here.)

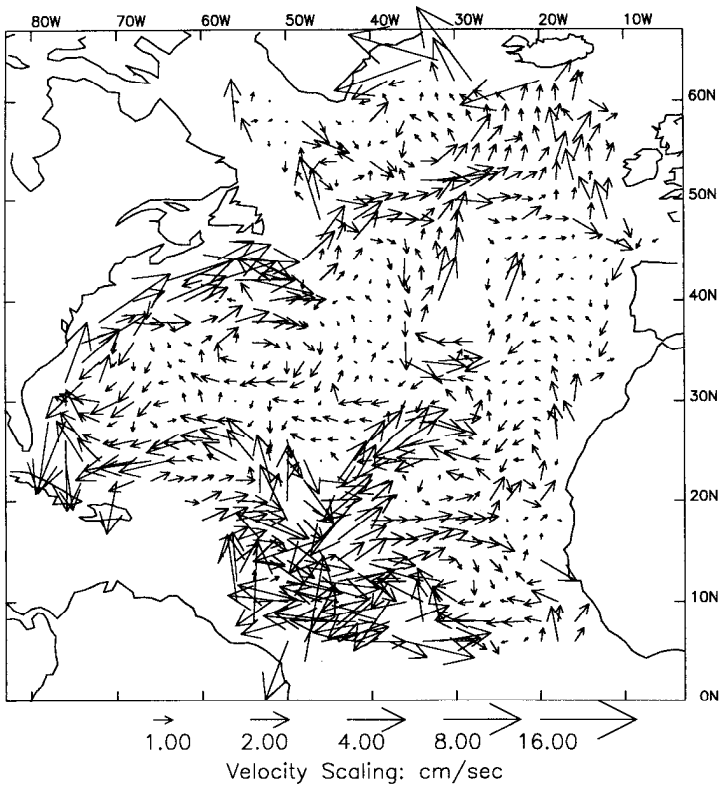

Figure 6. **u** at 1000 m for ψ(east) = 0 solution. Vector scaling is linear for speeds less than 1 cm/sec. Vector scaling is logarithmic for speeds greater than 1 cm/sec. Scale vectors appear below plot.

Despite differences in methodology, the major features from Mellor *et al.* (1982) are reproduced with our implementation of the ψ(east) = 0 criterion. These similarities include the front-like features.

The minimum-mixing ψ (Fig. 5) has $F(f/h)$ selected to minimize B_0 as described in Section 2d. The minimum-mixing ψ is smoother than the ψ(east) = 0 solution. There are prominent differences associated with the front-like features mentioned above. In particular, there is no indication of transport around the shadow dome, and the large-amplitude feature along 20N in the ψ(east) = 0 solution has disappeared. In the minimum-mixing solution most of the large-gradient features south of 20N are concentrated near the eastern boundary.

c. Horizontal velocity. In both the ψ(east) = 0 and minimum-mixing solutions, near-surface **u** is well approximated by the dynamic method in which **u** is estimated by integrating the geostrophic shear from some great depth where the flow is arbitrarily taken to vanish. In both cases, the sub-thermocline (deeper than roughly

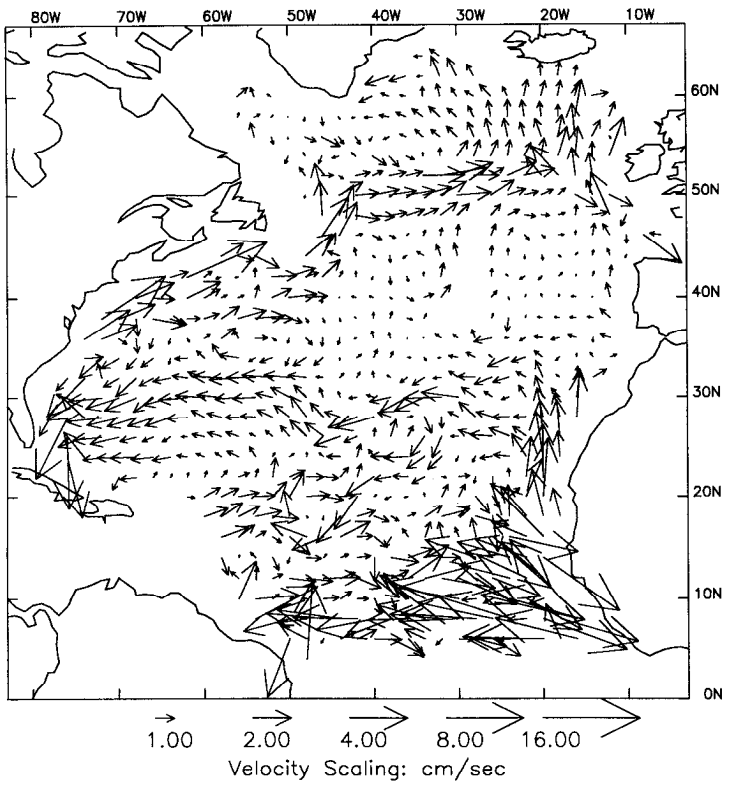

Figure 7. **u** at 1000 m for minimum-mixing solution. Vector scaling as in Figure 6.

700 m) velocities are as much as an order of magnitude smaller than the surface velocities. The surface velocity field is therefore reasonably independent of the allowed variations in $F(f/h)$. Below the thermocline, however, **u** is relatively sensitive to free-mode variations.

The 1000 m **u** field for the ψ(east) = 0 solution is presented in Figure 6. Along the western boundary north of 30N, there is poleward flow which turns north-eastward near 40N. This is characteristic of the Gulf Stream and its extension into the North Atlantic current. The two features that distinguished ψ fields above are evident in **u** as well. There are currents as large as 2 cm/sec flowing cyclonically around the shadow dome in the ψ(east) = 0 solution, and larger-amplitude flows parallel to f/h contours along 20N.

The 1000 m minimum-mixing velocity field is presented in Figure 7. It is much smoother than the ψ(east) = 0 flow in Figure 6. In contrast with the ψ(east) = 0 solution, the flows along 20N and around the shadow dome are relatively weak. The minimum-mixing solution is distinguished by westward flow across the entire mid-ocean basin from 25N to 33N. This westward flow is one of the more interesting predictions of the minimum-mixing model for reasons discussed in Section 6.

Horizontal flow in the front-like features is fairly depth-independent below the thermocline. For the ψ(east) = 0 solution, bottom horizontal velocity $\mathbf{u}_b$, and $\mathbf{u}$ at 1000 m have most of the same large-amplitude features (see Bogden, 1991, Fig. 3.6), including flow around the shadow dome and front-like flows near 20N. The bottom flows we compute for the ψ(east) = 0 solution reproduce the major features presented by Mellor *et al.* (1982) in their Figure 15. (They do not present mid-depth $\mathbf{u}$.)

Whereas sub-thermocline $\mathbf{u}$ in the ψ(east) = 0 solution is fairly depth-independent, mid-depth and abyssal $\mathbf{u}$ in the minimum-mixing solution are markedly different. Minimum-mixing $\mathbf{u}_b$ (Fig. 8) tends to align with isobaths, along the lateral boundaries and Mid-Atlantic Ridge, with shoaling bathymetry to the right of $\mathbf{u}_b$.

d. Vertical velocity. Vertical velocity at 1000 m for the ψ(east) = 0 solution is plotted in Figure 9. The largest values occur along the western boundary, where $|w| > 10^{-3}$ cm/sec. Values exceeding 10^{-3} cm/sec also appear in the mid-ocean near the shadow dome and along 20N. These vertical flows are associated with the front-like features in $\mathbf{u}$ and ψ. The vertical flows are largest where $\partial h/\partial x$ is large, indicating that they are sensitive to free-mode variations. As discussed below, these large w's require unreasonably large cross-isopycnal flows. Thus w provides an important diagnostic of the unrealistic character of the frontlike features. Mellor *et al.* (1982) did not present w.

The 1000 m minimum-mixing w (Fig. 10) is remarkably different from the ψ(east) = 0 solution. The front-like features near the shadow dome and along 20N are much less apparent in the minimum-mixing solution; the largest mid-ocean w's in Figure 10 have less than half the magnitude of those in Figure 9. Also, while both solutions have large values along the western boundary, only the minimum-mixing solution has equally large values along the eastern boundary.

Bottom w for both the ψ(east) = 0 and the minimum-mixing solutions exhibits general patterns that are similar to w at 1000 m, although $|w_b|$ is generally larger (see Bogden, 1991, Figures 3.10 & 3.11). In particular, w_b associated with the mid-ocean front-like features near 20N is 4 to 5 times larger than the same features at 1000 m. As a function of depth, $|w|$ in the front-like features increases nearly linearly from w_e of $O(10^{-5}$ cm/sec) at the surface, to values of $|w_b|$ that are nearly two-orders of magnitude larger.

e. Mixing. The minimum-mixing solution selects $F(f/h)$ to minimize the weighted integral (27) of the square of "mixing" defined as $\mathbf{u} \cdot \nabla\theta + w\partial\theta/\partial z$, where θ is locally referenced potential density. The resulting horizontal and vertical contributions to "mixing" at 1000 m are plotted in Figures 11 12, respectively, for the minimum-mixing solution. Vertical advection, $w\partial\theta/\partial z$, dominates horizontal advection, $\mathbf{u} \cdot \nabla\theta$,

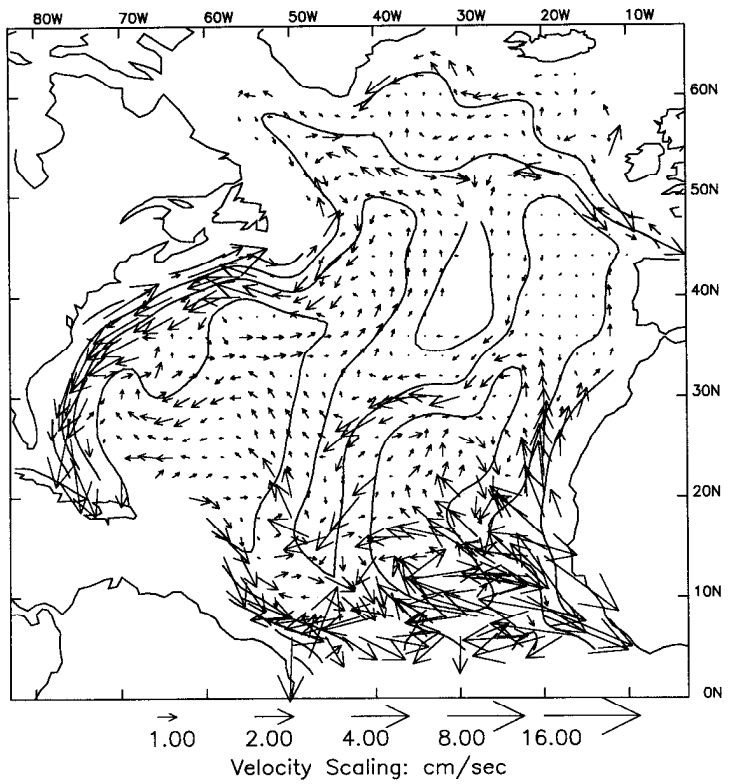

Figure 8. $\mathbf{u}_b$ for the minimum-mixing solution superposed on bathymetry plotted with contour interval of 1 km. Vector scaling as in Figure 6.

by nearly an order of magnitude over most of the domain. (The dominance of this term is even more pronounced for the ψ(east) = 0 solution.) Therefore, apart from a change in sign, w and mixing are similar. The horizontal term only becomes comparable to the vertical term near the lateral boundaries, where both terms are as much as 10 times larger than in the interior. (Because the boundary regions do not contribute to B_0 in the minimum-mixing solutions, the largest values in Figures 11 and 12 have no impact on free-mode selection.) Since $w\partial\theta/\partial z$ dominates $\mathbf{u} \cdot \nabla\theta$ in the mid-ocean, the minimum-mixing solution corresponds very nearly to the solution with minimum mean-square w.

5. Optimizing density

Free-mode selection based on the minimum-mixing criterion reduces front-like features because associated mid-depth w's require large cross-isopycnal velocities. Still, residual w's are large enough that $|w\partial\theta/\partial z| \gg |\mathbf{u} \cdot \nabla\theta|$. For the flow to remain approximately along isopycnals, these terms must have comparable magnitudes. The

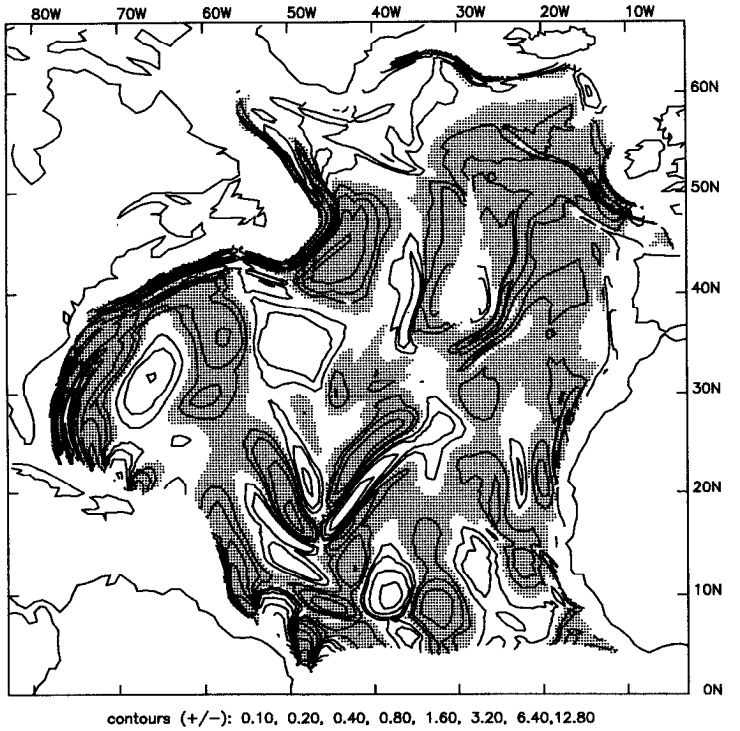

Figure 9. *fw* at 1000 m for ψ(east) = 0 solution. Shaded areas are negative values and correspond to downward velocity. In units of 10^{-7} cm/sec^2, contours are: $+/-0.1$, 0.2, 0.4, 0.8, 1.6, 3.2, 6.4. (Note, $f = 10^{-4}$/sec at 43N.)

objective of this section is to investigate the possibility that these large residuals may be attributable to errors in ρ and h, as discussed in Section 2c.

Small-amplitude adjustments to ρ are optimized to further reduce mixing in order to create dynamically "compatible" data. This can be accomplished either by adjusting smooth ρ to be compatible with smooth h or vice versa. We choose to vary ρ while leaving h fixed because the dynamics are linear in ρ but non-linear in h. (Varying h changes the characteristics of the hyperbolic equation.) Also, the analysis of Section 2c shows that plausible errors in ρ are likely to have larger dynamical impact in the mid-ocean than plausible errors in h. Although τ_0 remains fixed as well, results show that the dynamical impact of ρ adjustments is larger than could be accounted for by plausible errors in τ_0.

a. Density adjustments. Adjustments to ρ are represented by a linear combination of smooth analytic functions.

$$\tilde{\rho}(\mathbf{x}) = \sum_k a_k R_k(\mathbf{x}). \tag{42}$$

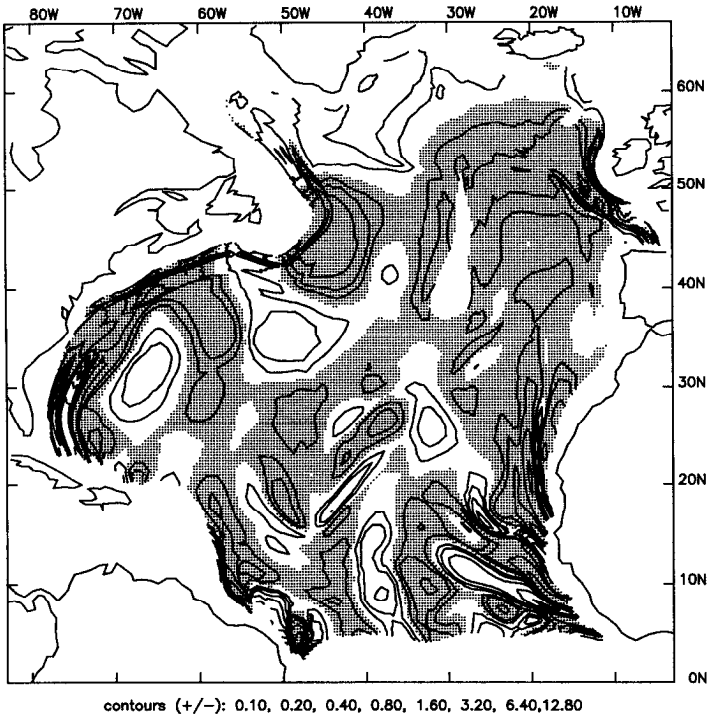

Figure 10. *fw* for the minimum-mixing solution. Contours as in Figure 9.

Adjusted density is $\rho + \tilde{\rho}$. The representers, R_k, for $\tilde{\rho}$ are sines and cosines with wavenumbers that vary uniformly from zero to roughly one cycle in 7 degrees of longitude and latitude. This choice of representers automatically enforces horizontal smoothness in $\tilde{\rho}$. The functional representation is used to evaluate $\tilde{\rho}$ at grid points. Once these values are determined, ρ and $\tilde{\rho}$ are interpolated between grid points according to the algorithm described in Section 3.and

The vertical structure of $\tilde{\rho}$ affects the problem in three ways. First, bottom flow and the transport $\mathbf{U}_b$ are affected by $\mathbf{U}_s$ through the integral $\int_h^0 z\nabla\rho\, dz$. Second, the minimum-mixing criterion depends on a similar integral from $z = -h$ to the level where mixing is defined, here 1000 m. Third, after $\mathbf{U}_b$ is determined, $\nabla\rho$ affects the geostrophic shear. Here, two vertical structures are examined. One adjustment is independent of depth, the other has different depth-independent fields $\tilde{\rho}$ above and below 1000 m, each field having the form (42).

To find $\tilde{\rho}$, the amplitudes, a_k, and the free mode, $F(f/h)$, are varied simultaneously to minimize mixing while keeping the density adjustments small. This is done by minimizing

$$\tilde{B} = B_0 + \lambda \iint |\tilde{\rho}|^2 \, d\mathbf{x} \tag{43}$$

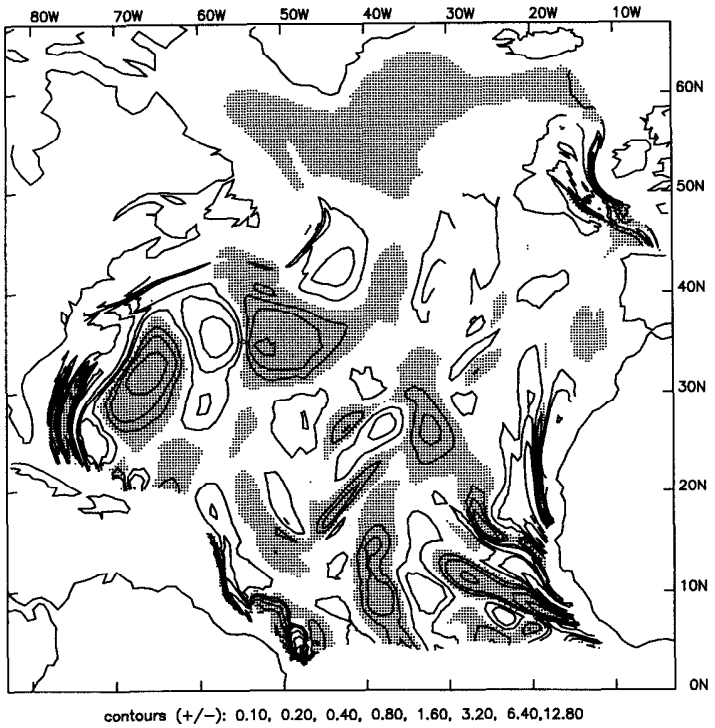

Figure 11. *fw* $\partial\theta/\partial z$ for the minimum-mixing solution. Contours as in Figure 9 with units 10^{-15} gm/cm^{3}sec^2.

where B_0 is the same measure of mixing defined in (27). The weights λ are adjusted to keep $\tilde{\rho}$ appropriately small. For the depth-independent $\tilde{\rho}$, only one λ is needed. While $\tilde{\rho}$ is adjusted, the advected tracer θ is unchanged, keeping the optimization problem linear. This is reasonable because the vertical advection term dominates B_0 and it would be unreasonable to minimize mixing by reducing $\partial\theta/\partial z$.

b. The size of 'reasonable' adjustments to ρ. In varying ρ, the objective is to keep the adjustments small enough to be attributable to errors in the data. Small size is important since the adjustments will be made without regard to the original unsmoothed data. Unfortunately, the errors associated with Levitus' (1982) smoothing analysis are not well known. The only statistical information accompanying the Levitus data set are 5°-square computations of average, standard deviation and number of observations. Standard deviations in thermocline-depth temperature are as large as 4°C near the western boundary and as low as 0.3°C in other areas. At 4000 m, standard deviations of 0.05°C are typical. Thermocline-depth salinity has standard deviations ranging from 0.5 to 0.05 PSU, with 4000 m values ranging from 0.05 to 0.02 PSU.

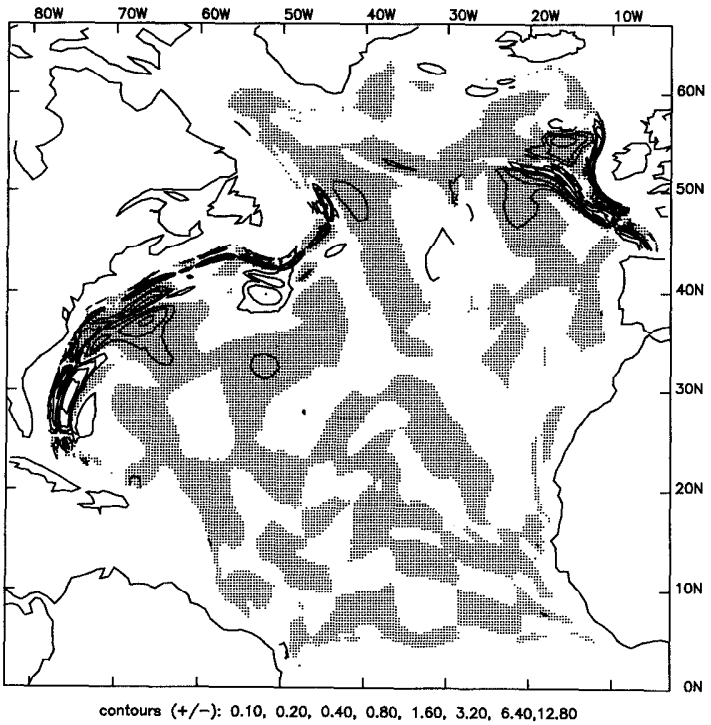

Figure 12. $f\mathbf{u} \cdot \nabla\theta$ for the minimum-mixing solution. Contours as in Figure 11.

These values have little bearing on the expected errors of the analyzed fields, which were computed from the data using an iterative smoothing technique with a data-dependent smoothing scale. Olbers *et al.* (1985) estimated errors in Levitus' fields by assuming a constant smoothing scale of 1000 km. They recognized that their method underestimated total error by assuming that sampling errors were uncorrelated. Therefore, they presumed lower bounds of .02°C and .02 PSU for temperature and salinity errors, respectively.

For typical values of thermal and haline expansion coefficients, a 0.02°C temperature change corresponds to a density change of 5×10^{-6} gm/cm^3, and a 0.02 PSU change in salinity corresponds to a density change of 15×10^{-6} gm/cm^3. An abyssal density error larger than 20×10^{-6} gm/cm^3 is probably unreasonable. At thermocline depths however, errors of 20×10^{-6} gm/cm^3 are probably small. These values are used as rough guides to bound the size of $|\tilde{\rho}|$.

c. Experiment #1: Depth-independent adjustments. In the first experiment, $\tilde{\rho}$ represents a depth-independent adjustment of the entire water column, and λ is chosen so that typical $\tilde{\rho}$ amplitudes are $O(10 \times 10^{-6}$ gm/cm$^3)$. In total, 220 different representers, R_k, are used.

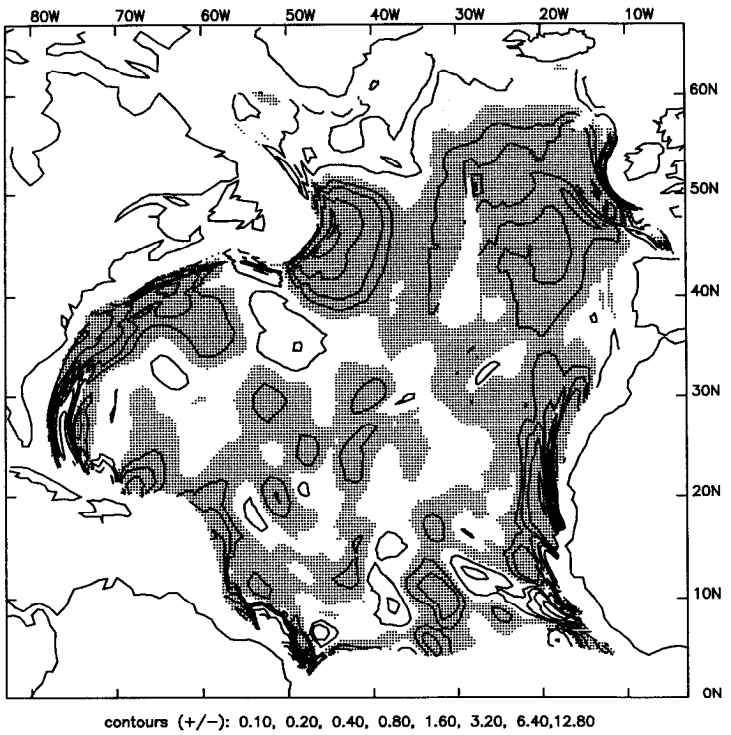

Figure 13. *fw* at 1000 m for minimum-mixing solution in Experiment #1. Contour intervals as in Figure 9.

The resulting 1000 m vertical velocity field is plotted in Figure 13 with the same scaling as in Figures 9 and 10. Large-scale features in w are reduced in magnitude by about a factor of two, and any remaining mid-ocean front-like features have disappeared. Near the boundaries, where advective misfit is not penalized, w's are the same as before. As in the previous section, patterns of w and mixing at 1000 m are similar because the vertical advection term still dominates.

Whereas vertical velocity is sensitive to the $\tilde{\rho}$ adjustment, $\mathbf{u}$ at 1000 m is relatively robust (Fig. 14). Large-scale features in $\mathbf{u}$ are similar to the minimum-mixing solution without density adjustment (Fig. 7). Differences in mid-ocean are limited to small scale features. The largest changes occur along 20N and near the eastern boundary south of 20N. Effects on w_b and $\mathbf{u}_b$ are similar to their 1000 m counterparts.

The density adjustments $\tilde{\rho}$ (Fig. 15) are dominated by fairly small scales. East-west scales tend to be smaller than the meridional scales. Otherwise, there is no clear spatial pattern to the adjustments.

d. Experiment #2: Depth-dependent adjustments. In this experiment, density is adjusted independently above and below 1000 m using a total of 440 different R_k. The shallow and deep adjustments are weighted differently with $\lambda_{deep} = 100\lambda_{shallow}$ to

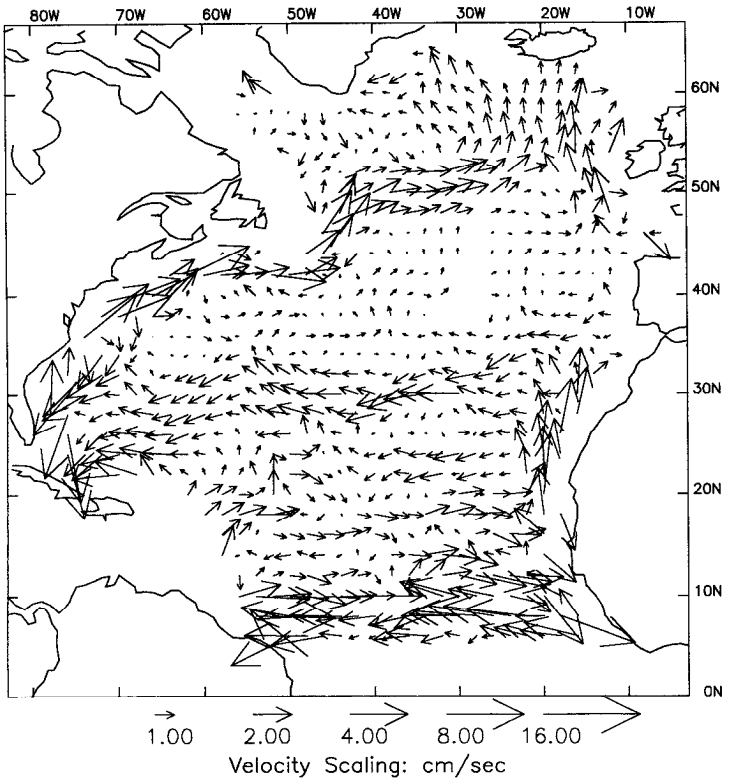

Figure 14. **u** at 1000 m, for minimum-mixing solution in Experiment #1. Vector scaling as in Figure 6.

reflect larger expected errors at thermocline depths. Values of λ_{deep} and $\lambda_{shallow}$ are chosen so that adjustments in both layers are comparable to measurement errors.

The resulting field of w is similar to that in Experiment #1. The values near the shadow dome (40N, 30W) are somewhat larger, while mid-ocean values south of 30N are slightly smaller. The 1000 m horizontal velocity field also differs only in small details from its counterpart in Experiment #1. The horizontal velocity field from this experiment is described in detail in the comparison with observations in Section 6.

The primary difference from Experiment #1 is that adjustments in this case are more easily attributable to data errors. The $\tilde{\rho}_{deep}$ field has about half the root-mean-square amplitude of the depth-independent $\tilde{\rho}$ in Figure 15, although scales and patterns are similar. The shallow adjustments $\tilde{\rho}_{shallow}$ are about 5 times larger than those in Figure 15 with similar scales but different patterns. The shallow adjustments are still small compared to the relatively large expected errors at thermocline depths.

e. Experiment #3: Including the lateral boundaries. This experiment involves shallow and deep density adjustments as in Experiment #2. Here, however, the domain for

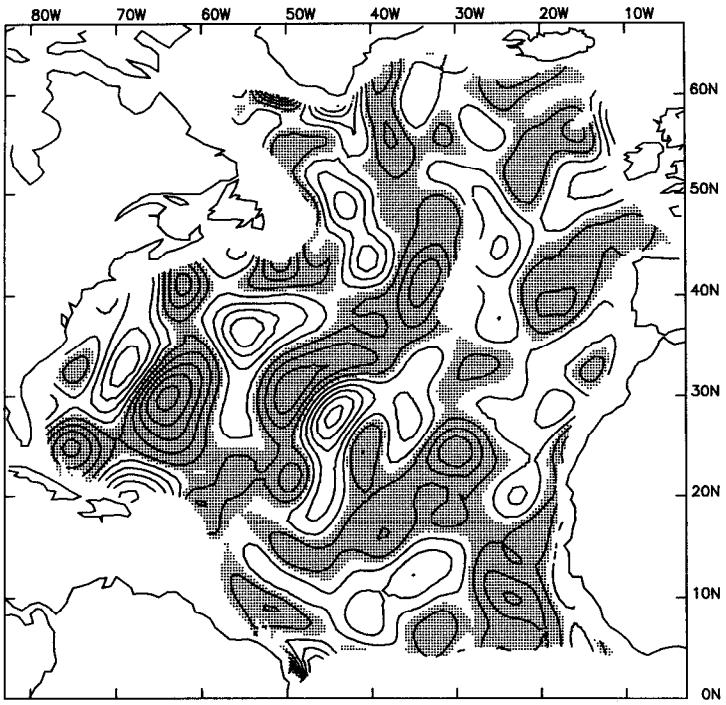

Figure 15. $\tilde{\rho}$ for Experiment #1, Contour interval: 2×10^{-6} gm/cm^3. Negative values are shaded. Contour values are offset by ½ contour interval from zero so that zero contour is not plotted.

evaluating B_0 includes the boundaries. Values of λ_{deep} and $\lambda_{shallow}$ are selected so that the mid-ocean mixing compares with values in Experiments #1 and #2.

The resulting mid-ocean w's at 1000 m (Fig. 16) compare closely with previous experiments. Striking differences occur along the boundaries, however, where front-like features in w have been dramatically reduced. Boundary values are still relatively large, but they have diminished by as much as an order of magnitude in some areas.

The 1000 m horizontal velocity field (Fig. 17) has many of the features of the previous solutions, even along the boundaries. The same is true for the bottom velocity $\mathbf{u}_b$, which has slightly stronger along-isobath flow around the shadow-dome region. (Note, the sense of this flow around the shadow dome for all minimum-mixing solutions is opposite that in the ψ(east) = 0 solution.)

Density-adjustment amplitudes in this case are about a factor of 2 larger than those in experiment #2. This is as large as we consider reasonable given the ignorance of the unsmoothed data. Shallow density adjustments tend to be largest near the western boundary.

North of 20N, the transport streamfunction for this problem (Fig. 18) is similar to unadjusted ψ (Fig. 5) but density adjustments result in slightly smoother ψ, particularly near the boundaries.

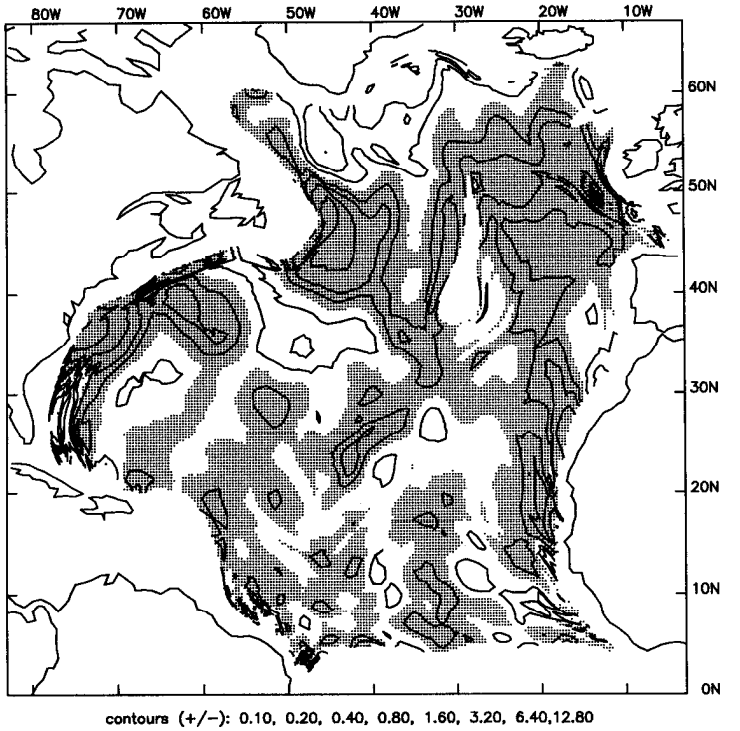

Figure 16. *fw* at 1000 m for Experiment #3. Contours as in Figure 9.

f. Dynamical impact of ρ *adjustments.* Amplitudes of density adjustments, $\tilde{\rho}$, are small enough to be attributable to expected errors, with horizontal variation comparable to the smoothing scales. Their local dynamical impact can be measured with (11), rewritten here

$$\mathbf{U}_b \cdot \nabla(f/h) = \frac{1}{h}(\mathbf{U}_s \cdot \nabla f + fw_e). \tag{44}$$

Both terms on the right are computed from ρ, h and τ_0. $\mathbf{U}_s \cdot \nabla f$ (Fig. 19) typically dominates fw_e by nearly an order of magnitude. Large-scale features in $\mathbf{U}_s \cdot \nabla f$ computed from $\rho + \tilde{\rho}$ are similar. There are distinct differences on smaller scales, however, particularly south of 40N.

The contribution to $\mathbf{U}_s \cdot \nabla f$ due solely to $\tilde{\rho}$ from Experiment #2 is plotted in Figure 20. The dominance of shorter zonal scales result from the fact that

$$\mathbf{U}_s \cdot \nabla f = \hat{\mathbf{z}} \cdot \nabla f \times \frac{g}{f} \int_{-h}^{0} z \, \nabla \rho \, dz \tag{45}$$

is a weighted vertical integral of the zonal density gradient. (The factor of $1/f$ is partly responsible for larger values near the equator.) The dynamical impact of $\tilde{\rho}$ is also

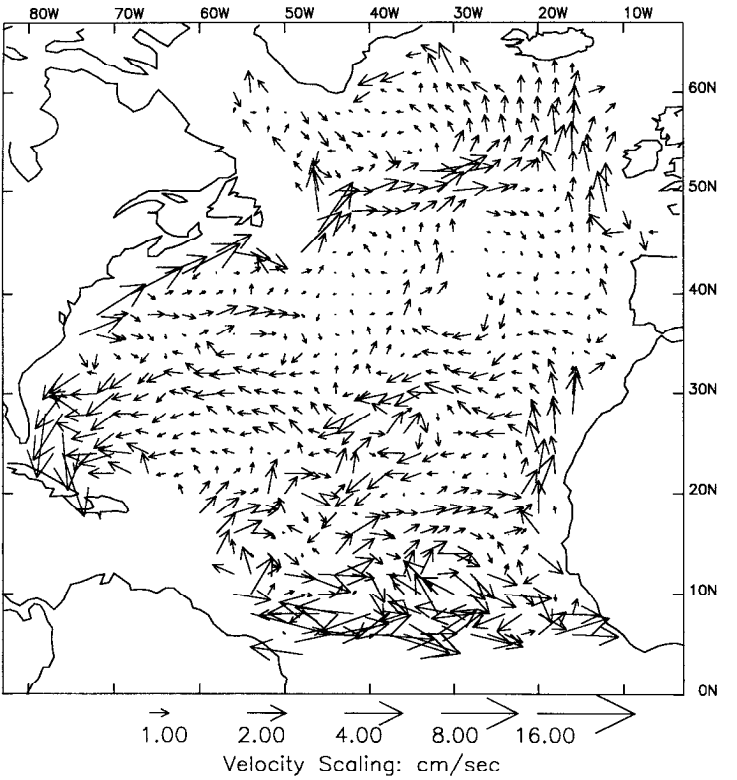

Figure 17. **u** at 1000 m for Experiment #3. Vector scaling as in Figure 6.

much larger, with smaller scales, than the contribution from fw_e. While wind-stress estimates are subject to a variety of error sources (see Hellerman and Rosenstein, 1983), it is highly unlikely that plausible errors in τ_0 could affect fw_e by as much as $\tilde{\rho}$ affects $\mathbf{U}_s \cdot \nabla f$.

6. Comparison with observations

The analysis of Section 5 shows that minimum-mixing w is particularly sensitive to errors in ρ. In contrast, **u** is relatively robust. The purpose of this section is to compare the robust predictions with independent evidence of the general circulation. Results are compared to direct observations of the time-averaged horizontal currents. Reliable measurements of the mean **u** are rare however, because of energetic variability with relatively short time scales. Therefore, much of the discussion focuses on comparing the predicted flows to notions of the circulation that have been obtained from descriptive studies of property distributions. The predictions provide a framework for explaining property distributions in terms of advection by the time-averaged circulation.

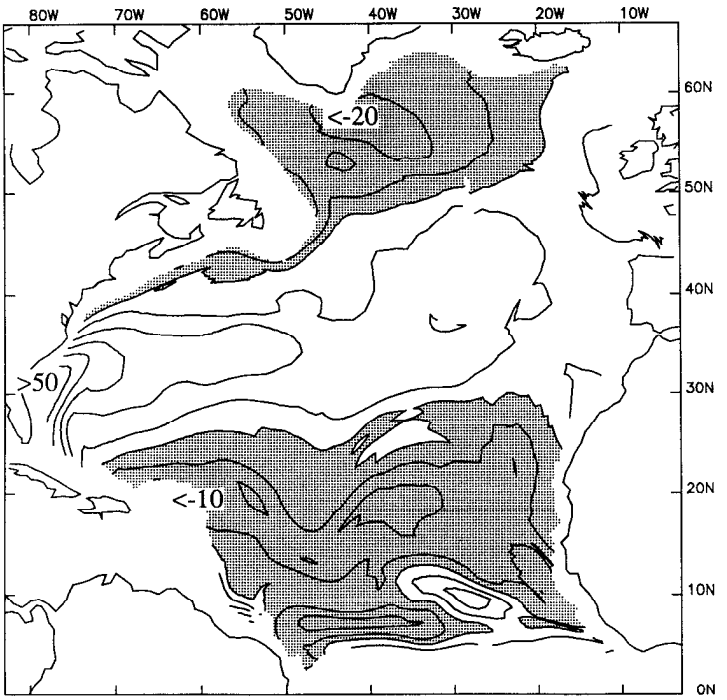

Figure 18. Streamfunction ψ for Experiment #3. Contour interval as in Figure 4. Note: ψ is determined up to an arbitrary constant.

In this test of the model, two aspects of the predicted flow field are of particular interest. The first is a strong mid-depth westward flow across the North Atlantic in a fairly narrow range of latitude, between roughly 25N and 33N. The second is a tendency for $\mathbf{u}_b$ to align with isobaths so that shallow water lies on the right.

The predicted velocities described below come from the minimum-mixing solution obtained in Experiment #2 of Section 5. The major features described below show up consistently in the minimum-mixing solutions presented in the previous sections, both with and without density adjustments. We consider details of the predicted flows to be suspect near the lateral boundaries, where data-error sensitivities are greatest and model errors are also likely to be relatively large.

a. Near-surface flow. The purpose of describing the near-surface flow field is twofold. First, it demonstrates the expected result that the near-surface horizontal flow is well approximated by the dynamic method, i.e. by vertically integrating the geostrophic shear from some depth below the thermocline where the flow is arbitrarily set to zero. Second, comparing surface flows computed from smoothed and unsmoothed data shows that smoothing has eliminated some persistent features in the data. The effects of smoothing are particularly apparent near the lateral boundaries.

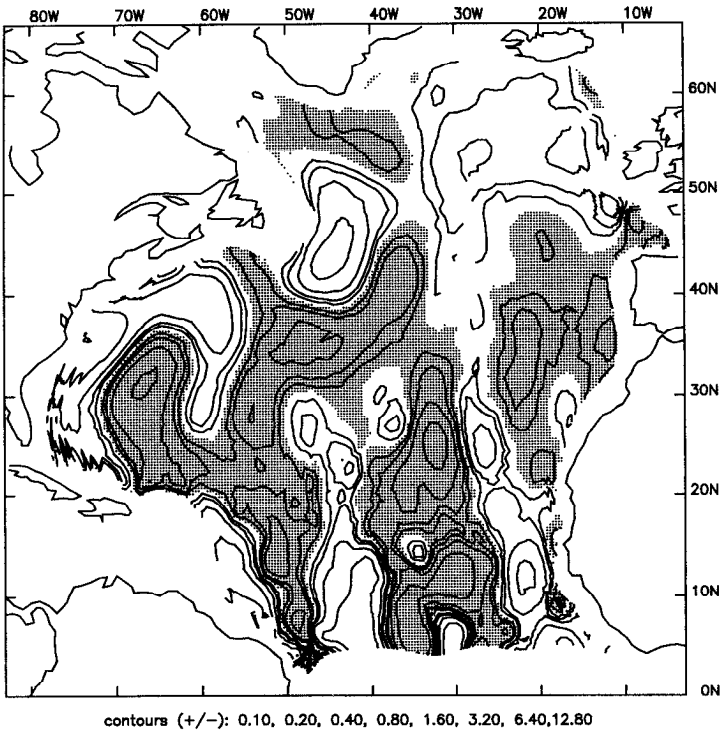

Figure 19. $\mathbf{U}_s \cdot \nabla f$ for unadjusted ρ. Contours as in Figure 9.

The minimum-mixing surface pressure is plotted in Figure 21. This plot is nearly identical to surface pressure relative to zero at 1000 m, or any other depth below the main thermocline (see Bogden, 1991).

Figure 21 can be compared to dynamic height at the sea surface relative to the 1000-dbar surface from Reid (1978). The contour intervals are comparable. (In the ocean, the difference between dynamic height and the vertical integral of $\partial p/\partial z = -\rho g$ is of order $|\rho_0 - \rho|/\rho_0 \approx 10^{-3}$, where ρ_0 is a mean density.) The major differences are attributable to smoothing and, to a lesser extent, to different data sets. Reid used a high-quality subset of the data used by Levitus (1982).

North of 10N and away from the lateral boundaries, the large scale features in Figure 21 are comparable to those in Reid's result. The most prominent differences are associated with the Gulf-Stream and North-Atlantic Current system. The tortuous contours in the western North Atlantic in Reid's result may reflect the variable nature of the geostrophic currents or highly structured mean flows. In any case, the time and space averaging used by Levitus (1982) has resulted in a heavily smoothed version of the geostrophic shear. In particular, the classical mid-latitude "C-shaped" circulation (Reid, 1978) is almost removed in the smoothed data. Important differences occur along the ocean boundaries as well. Many of the

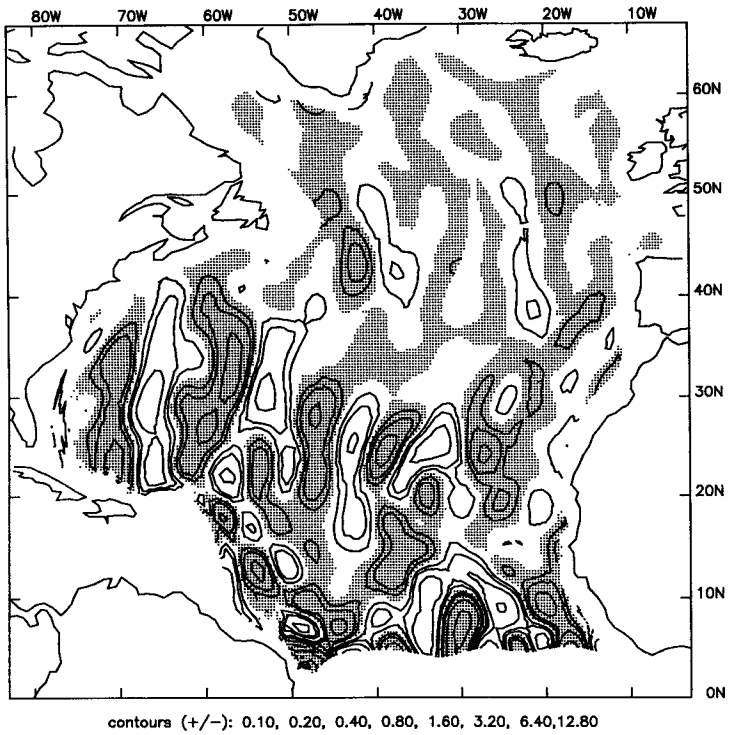

Figure 20. $\mathbf{U}_s \cdot \nabla f$ computed from $\tilde{\rho}$ in Experiment #2. Contours as in Figure 9.

small-scale boundary features presented by Reid represent persistent patterns that are not included in the smoothed density field used here. These patterns are associated with known current systems such as the Labrador Current, along the boundary of the Labrador Sea, and the poleward-flowing Antilles Current near the Caribbean (e.g. Sverdrup *et al.*, 1942). Reid's result also has narrower and more intense poleward relative flows near 45N, 40W and equatorward flows near the coast of Northern Africa. Similar comments apply to comparisons with dynamic height calculations of Leetmaa *et al.* (1977) and Tsuchiya (1985).

b. Mid-depth flow and the Mediterranean salt tongue. Compared to the near-surface flow, mid-depth flow in the North Atlantic is poorly known. Inference based solely on the dynamic method provides little insight on velocity because the assumed reference levels are unreliable, even as approximations, below the thermocline. Also, directly measured currents fail to provide a unified picture of the circulation because of their sparseness and the uncertainty resulting from their variability.

The most tantalizing evidence of a time-averaged circulation comes from the property distributions. The salinity distribution in particular has motivated a variety of conflicting circulation schemes outlined below. Our calculations propose a resolu-

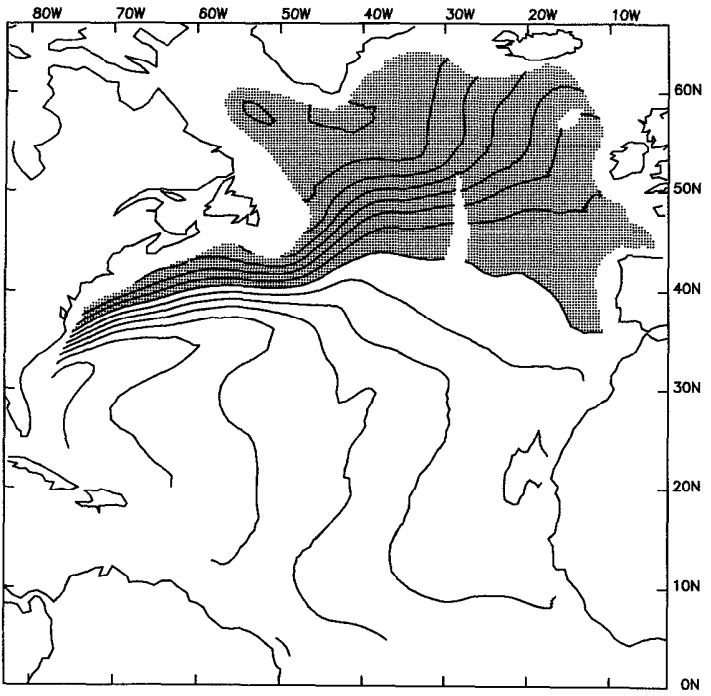

Figure 21. Surface pressure (divided by 1 gm/cm^3) for minimum-mixing solution from Experiment #2 in Section 5. Contour interval: 10^{-4} cm^2/sec^2.

tion to the controversy that is consistent with the directly observed currents. The predictions provide a framework for understanding the role of the time-averaged circulation in maintaining the salinity distribution. In particular, our results support an early conjecture by Wüst (1935).

The Mediterranean salt tongue is the most prominent mid-depth tracer distribution in the North Atlantic. Highly saline effluent from the Mediterranean accounts for a vertical maximum in the salinity field at 1000–1200 m depth across the entire North Atlantic. Reid (1978) describes this feature and cites some of the earliest references.

Controversy over the salt tongue concerns the relative importance of advection and mixing in the maintenance of the salinity maximum. For example, Wüst (1935) proposed a westward downgradient "spreading" along the maximum of the tongue-like salinity feature, originating near the Straits of Gibraltar. This interpretation requires mixing if salinity is to be conserved, otherwise flow must be along salinity isolines. Reid (1978) proposed a slightly different interpretation of the circulation based on the salinity distribution and the dynamic method, using the assumption that the flow at 2000 m is smaller than at 1000 m. Reid placed the salt tongue at the center of a "C-shaped" circulation that flows westward along the northern flank of the

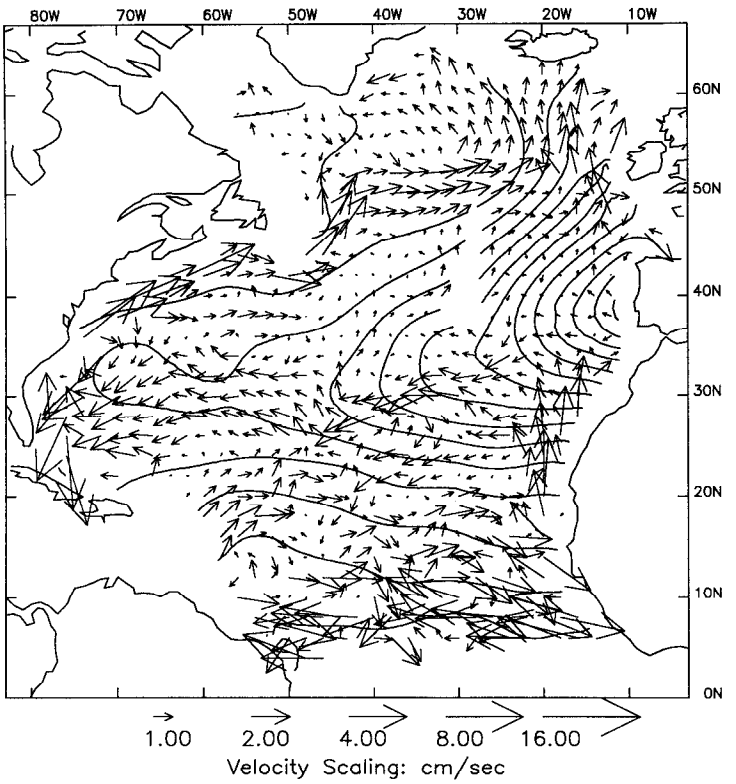

Figure 22. **u** at 1000 m for minimum-mixing solution from Experiment #2 in Section 5. Vectors superposed on salinity at 1000 m from Levitus (1982) plotted with contour interval: 0.1 PSU. Vector scaling as in Figure 6.

tongue and eastward on the southern flank, with flow approximately along salinity isolines. The westward flows suggested by both Wüst and Reid are consistent with generally accepted notions of a large-scale mid-latitude gyre. Worthington (1976) proposed an altogether different scheme. The existence of the salt tongue extending across the Atlantic led Worthington to abandon the concept of a large-scale circulation extending across the basin at mid-depth. His scheme isolated the mid-depth circulation in the western basin, and avoided flowing through the salinity-maximum feature altogether.

Our results predict strong, O(1cm/sec), westward flow along the salt tongue across the entire North Atlantic. This is clear in Figure 22 showing the predicted 1000 m velocity superposed on contours of salinity at 1000 m from Levitus (1982). The mid-ocean westward currents lie in a narrow range of latitude between 25N and 33N. Flow along the tongue supports Wüst's (1935) conjecture and the recent interpretation of Reid (personal communication). There is strong westward flow in the solutions at 2000 m as well. Figure 23 shows the 2000 m velocity vectors and salinity

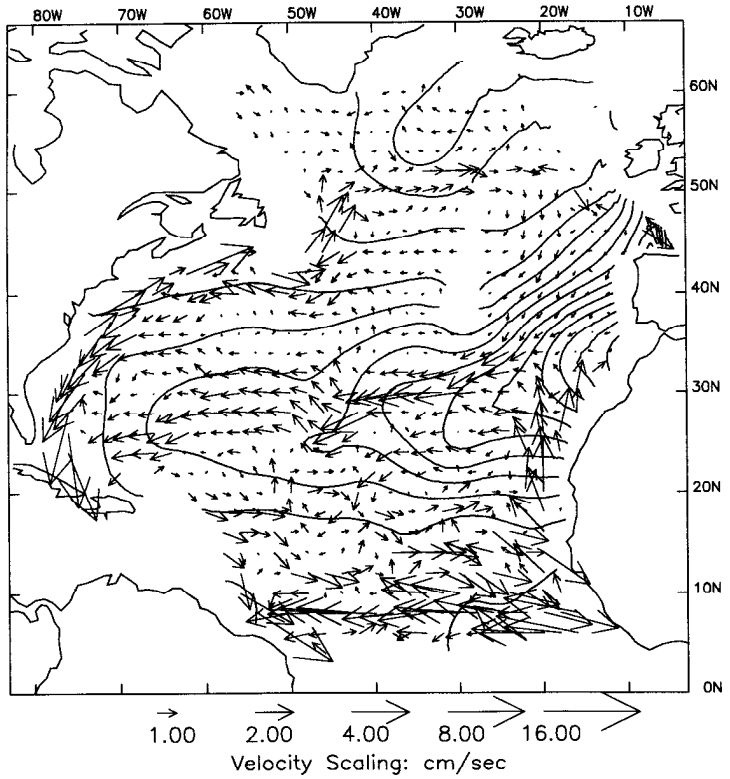

Figure 23. **u** at 2000 m for minimum-mixing solution in Experiment #2 in Section 5 superposed on salinity at 2000 m from Levitus (1982) plotted with contour interval 0.02 PSU. Vector scaling as in Figure 6.

contours. The salt tongue is still evident at this depth, although the gradients are smaller in magnitude.

Measurements of horizontal velocity corroborate the prediction. Several sets of measurements have been obtained in the latitude range where the results exhibit strongest westward flow. These are included in Figure 24, which shows a compilation of results from 1000–2000 m depth. Vectors are scaled the same as those in Figures 22 and 23. The measurements are discussed below.

We focus first on the measurements near 30N. Two current-meter mooring clusters in the central North Atlantic at 27N and 28N are of particular interest. The moorings were deployed as part of the POLYMODE experiment in the mid-1970's (Fu *et al.*, 1982). Cluster A (28N, 48W) and Cluster B (27N, 41W) were set on the western and eastern flanks, respectively, of the Mid-Atlantic Ridge. Each vector represents a 1-year average at a nominal depth of 1500 m (the smallest vector in Cluster A represents the only available 2-year average). Westward flow predominates at both POLYMODE sites. One exception to westward flow occurred at the

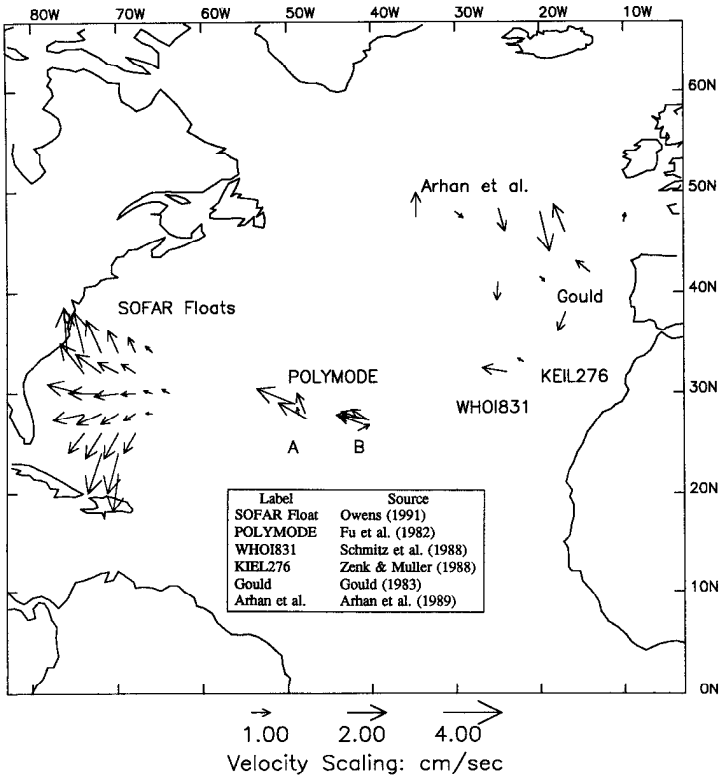

Figure 24. **u** at 1000 m to 2000 m for directly measured currents from a variety of different sources discussed in text. Vector scaling as in Figure 6.

southernmost mooring of Cluster B, where flow was toward the north-east. Comparison with Figures 22 and 23 shows good agreement with the prediction. Even the anomalous north-east vector at Cluster B coincides geographically with a flow reversal in the calculation (Fig. 22), although agreement on such small scale is undoubtedly fortuitous.

Farther to the east, near 25W, two more current vectors at 32N and 33N (Fig. 24) indicate westward flow at the depth of the salt tongue. These measurements also coincide geographically with the predicted westward flow. The smaller vector at 33N, 22W represents flow at 1000 m depth from a 7-year-long current-meter record, KIEL276 (Zenk and Müller, 1988). However, despite the long record length, Zenk and Müller determine that the time-average velocity is not significantly different from zero.

The measurement located 200 km to the southwest at 32N, 24W, WHOI831, represents a 2-year average from 1070 m (Schmitz *et al.*, 1988). Average flow at this depth was 1.2 cm/sec. Westward flow was also measured at 470 m (2 cm/sec) and at 3000 m (0.5 cm/sec).

Currents at both the KIEL276 and WHOI831 sites exhibited strong interannual variation. During October 1984 to October 1985, the WHOI831 record showed the strongest year-average westward flow. During the same period, westward flow at KIEL276 was relatively weak. In the following year, the second and final year for WHOI831, the roles were reversed; westward flow at WHOI831 was weak while the KIEL276 record had a relatively strong westward component. The KIEL276 and WHOI831 measurements indicate that strong mid-depth westward flow may be associated with a jet-like feature with a time-varying position (Zenk and Müller, 1988). Evidence of a jet-like feature was obtained with current-following SOFAR floats coincident with the WHOI831 record (Schmitz *et al.* 1988). Twenty-one floats were deployed over 15° of latitude near WHOI831. Float trajectories indicated that the strong westward flow occurred in a narrow range of latitude (approximately 2°) around 32N. Westward flow in our prediction may represent a time and space average of a variable jet that may have been measured in the WHOI/KIEL studies.

c. Mid-depth flow in the eastern basin. In the eastern North Atlantic, predicted flows exhibit a fair amount of horizontal and vertical structure. Our results show poleward flows at 1000 m along most of the eastern boundary north of 15N (Fig. 22). Along the coast of Africa, between 15N and 30N, poleward flow is strong and nearly depth independent below 1000 m. At the latitude of the Straits of Gibraltar, there is weak flow to the west. Poleward flow is evident north of 40N, and increases in magnitude north of 50N. In contrast with the 1000 m flow, the 2000 m eastern-basin flow between 35N and 50N is predominantly southward (Fig. 23).

Between 35N and 50N, direct measurements at 1500 m show an overall pattern of poleward flow near the eastern boundary and southward flow farther offshore. This pattern is intermediate between our 1000 m and 2000 m predictions. The velocity vectors north of 35N in Figure 24 represent a composite of current-meter averages from several sources. The four westernmost vectors along 48N represent averages of 2 to 4 years of data (Arhan *et al.*, 1989). The other vectors north of 35N represent averages over ½ to 2 years (see Gould, 1983). Spatial variability in the measurements is large, reflecting the low statistical reliability of the averages. However, a pattern of poleward flow near the coast and equatorward flow farther offshore is robust in the observations, and observed flows are generally stronger than in the predictions. The exception to this trend occurs at the westernmost mooring at 48N and 35W, on the western flank of the ridge, where both the predictions and measurements have poleward flow.

Distributions of salinity and other tracers led Reid (1979) to surmise poleward flow at the depth of the salinity maximum (1000 m) along the eastern boundary. Reid used maps of dissolved oxygen, salinity and silica on isopycnals (surfaces of constant potential density) as evidence for his argument. As is the case for salinity, oxygen and

silica also have extrema along the eastern boundary of the ocean. Unlike salinity however, the oxygen minimum and silica maximum lie farther to the south near 20N. Isopycnal distributions of these quantities show that the extrema extend poleward along the eastern boundary. This is evident in Reid's vertical section near the coast, which indicates poleward flow along the boundary past 60N into the Norwegian-Greenland sea. (These tracer distributions are confirmed in the recent meridional section described by Tsuchiya *et al.*, 1991.)

Our results exhibit poleward flow at 1000 m near the eastern boundary north of 45N (Fig. 22). At 2000 m, poleward flow north of 35N is not evident (Fig. 23). The indication of flow in the property distributions at 2000 m is less clear than at 1000 m. The same is true in general of the property distributions south of 35N. In the predictions however, poleward flow is relatively strong at 1000 m and 2000 m along the northwest coast of Africa. The analysis in Section 5 shows that these poleward flows are fairly robust, as are the associated large values of mixing. Large values of mixing are particularly noteworthy since the near-boundary flows in this region cross relatively large gradients in salinity (Figs. 22 and 23).

At 2000 m, the predicted mid-latitude flow in the middle of the eastern basin differs in character from that at 1000 m depth. Between 33N and 50N, results predict a broad ½ cm/sec equatorward flow (Fig. 23). Relative flow between 1000 m and 2000 m in this region is consistent with the vertical geostrophic shear from Reid (1978), with poleward flow at 1000 m relative to the flow at 2000 m. However, since there is strong southward flow at 2000 m, this shear simply causes the absolute flow at 1000 m to be relatively weak. The equatorward flow at 2000 m depth coincides with a 5° southward displacement of the salinity maximum relative to 1000 m. The southward displacement in the salinity tongue appears in the "core layers" defined by Wüst (1935) as well.

A variety of other tracers have been used to infer southward flow below 1000 m in the eastern basin. Wüst (1935) identified an oxygen maximum layer at roughly 2000 m depth with origins at higher latitude, the Middle North Atlantic Deep Water. Reid's (1979) isopycnal analysis also shows that underlying extrema of oxygen and silica extend southward from the northernmost latitudes to near 40N. The water mass immediately underlying the salt tongue in the eastern basin is Labrador Sea Water. In addition to its characteristic oxygen maximum, used by Wüst to identify Middle North Atlantic deep water, Labrador Sea Water is characterized by vertical minima in both salinity and hydrostatic stability. From these characteristics, Labrador Sea water can be traced southward from 50N to as far as 38N in the eastern basin (Pingree, 1973; Talley and McCartney, 1982; Tsuchiya *et al.*, 1991). Tsuchiya *et al.* (1991) identify a plausible mechanism for vertical mixing with the overlying Mediterranean salt tongue in order to explain why the distinctive characteristics are not apparent farther south.

d. Mid-depth flow in the northern North Atlantic. Our results predict a strong 1–2 cm/sec eastward current across the middle of the North Atlantic between 50N and 53N at 1000 m depth (Fig. 22). The 1000 m flow has the same character as the flow nearer the surface (Fig. 21), although the deeper flow has smaller magnitude and a somewhat smaller range of latitude. This eastward flow is a strong signal in the geostrophic shear; i.e. the 1000 m flow is well approximated using the dynamic method and assuming the flow closer to the bottom is zero.

At 1000 m depth, evidence of eastward flow along 50N comes from tracer distributions. Eastward flow along 50N has been proposed in a number of studies to account for eastward extension of Labrador Sea Water from the Labrador Sea into the eastern basin (e.g. Ivers, 1975; Talley and McCartney, 1982).

Kraus (1986) presents a modern description of the North Atlantic Current near the surface based on hydrographic measurements and surface drifters. He describes a fairly broad eastward flow across the North Atlantic near 50N, similar to the pressure field in Figure 21. At 350 m and 600 m, measured currents along 48N have a strong eastward component (Arhan *et al.*, 1989). Eastward flow at these depths is evident in the predictions as well, though with smaller magnitude (not shown). At 1000 m and below, measured currents from Arhan *et al.* (1989) have stronger north-south components (Fig. 24). In the predictions, the strongest eastward flows below 1000 m lie north of 48N.

e. Mid-depth flow in the western basin. In the western North Atlantic, the most prominent mid-depth feature in the predictions away from the boundary is the westward flow south of 33N. North of 33N, the flow is spatially more variable. At 1000 m, there is an eastward flow between 35N and 40N (Fig. 22). but no eastward flow is apparent at 2000 m (Fig. 23).

A large number of current measurements have been made in the western North Atlantic. At mid-depth, however, the nature of the time-averaged flow field remains uncertain. One reason is the relatively large variability in the time-dependent current field (e.g. Schmitz, 1984) and another is that the time-averaged currents have fairly small spatial scales (e.g., Schmitz, 1980). Various current measurements corroborate the predicted westward mid-depth flow in the western basin south of 33N. A 15-month-long current-meter record from 800 m depth at 31N and 69.5W shows mean southwestward flow of 2.4 cm/sec (Owens *et al.*, 1982). Current-following SOFAR floats at 2000 m depth, deployed near 30N and 70W, also indicated westward flow up to the boundary (Riser *et al.*, 1978). A composite estimate of the averaged currents from a more extensive SOFAR-float data base shows westward flow west of 68W and south of 33N (Rossby *et al.*, 1983). In this analysis, westward 700 m currents are as large as several cm/sec with slower flow at deeper depths.

The set of vectors west of 60W labeled "SOFAR Floats" in Figure 24 represents a heavily smoothed version of the float-derived velocity measurements at 1500 m from

Owens (1991). The vectors in the plot were computed with spatial smoothing radius of roughly 500 km, and by weighting measurements in inverse proportion to the standard errors provided by Owens (1991). The smoothing scale is comparable to that used by Levitus (1982) to obtain the hydrographic data used in this study. The smoothed float velocities indicate westward flow in the same latitude range as in the predictions (Fig. 22); magnitudes are comparable as well.

North of 33N, the comparison between predictions and direct observations is not as good. Schmitz (1980) presents the averaged mid-depth currents from 15-month current-meter records at 6 sites along 55W, between 28N and 38N. Near 32N the averaged currents are westward at 1 cm/sec or less. At 36N however, Schmitz describes a "jet-like" eastward flow of order 10 cm/sec. This large-amplitude current is found from 600 m to the bottom, and covers less than three degrees of latitude. At 38N the current flows in the opposite direction with nearly the same magnitude and about the same weak vertical shear.

These deep nearly depth-independent observed currents are not evident in our results. The predicted eastward flow between 35N and 40N is relatively weak (approximately 1 cm/sec) and decreases in magnitude at greater depths. The large observed shear between 36N and 38N is nearly barotropic. The model could predict it only as a large difference between $\mathbf{U}_b$ on different f/h contours. Once the bottom topography and density are smoothed, this is unlikely. We can only hope that the spatial average is correctly predicted.

Between 45W and 70W, the observed time-averaged near-surface Gulf Stream (e.g. Schmitz, 1980; Hogg, 1983) lies slightly north of the predicted eastward mid-depth flow at 38N (Fig. 22), following the 4000 m–5000 m isobath. North of the Gulf Stream, over the continental slope, hydrographic data provide evidence of an equatorward flow as a southward extension of cyclonic flow near the boundary of the Labrador Sea (e.g. Sverdrup *et al.*, 1942; Ivers, 1975).

This equatorward flow near the surface and north of the Gulf stream conflicts with the predictions at the edge of the computational domain. There is no equatorward flow along the boundary in the model, either at 1000 m (Fig. 22) or at the surface (Fig. 21). Instead, the predicted flow is strongly poleward. This apparent deficiency in the calculation could reflect inadequacies in the smoothed data fields because, as pointed out in the beginning of this section, the density field used here lacks expressions of the small-scale currents along the boundaries.

South of 40N, the predicted mid-depth equatorward flow along the western boundary is robust, and is corroborated by measurements. Riser *et al.* (1978) present trajectories of SOFAR floats at 1500 m that confirm the prediction. After a meandering westward drift from their deployment positions near 28N and 70W, the floats entered a relatively strong equatorward current that hugged the continental slope. Farther south, at 26.5N, current-meter observations show averaged equator-

ward mid-depth flow near the continental slope of up to 20 cm/sec (Rosenfeld *et al.*, 1989; Lee *et al.*, 1990).

Still farther south along the boundary, SOFAR-float trajectories indicate that the equatorward western boundary flow turns east along the northern edge of the Caribbean (Rossby *et al.*, 1983; Owens *et al.*, 1988). These measurements conflict with the predictions. Two deficiencies in the model may account for the discrepancy between predicted and observed currents. First, as pointed out above, smoothing errors in ρ are likely to be large in this area as there is no evidence of the Antilles Current in the geostrophic shear. Second, and perhaps more important, the bottom topography used here does not include shoaling associated with the Caribbean. Consequently, the f/h contours terminate near 20N and 70W instead of following the shallow bathymetry toward the southeast (Fig. 1). The fate of the large observed (Rosenfeld *et al.*, 1989; Lee *et al.*, 1990) and predicted (Figs. 5 and 18) southward along-f/h transport near 26.5N remains unclear from our results.

f. Deep flow in the eastern basin. Closer to the bottom, predicted horizontal flow is quite different from the flow at mid-depth. Along the major slopes in the bottom topography, flow tends to follow isobaths. This is apparent at 3500 m depth (Fig. 25) and on the bottom (Fig. 26). At mid-latitudes, $\mathbf{u}_b$ aligns with isobaths so that topography shoals to the right. The flow is poleward along the eastern boundary and western flank of the Mid-Atlantic Ridge, and equatorward along the western boundary and eastern flank of the ridge. At northernmost latitudes, flow follows the bathymetry from east west to west. Away from the western boundary, speeds along the bottom approach 1 cm/sec in some locations. The general patterns in the abyssal flow field are robust aspects of the calculation.

Several predictions are verified by direct current measurements, as discussed below. It is difficult to obtain an impression of the large-scale current field from near-bottom measurements, however, because time-averaged flows near the bottom tend to follow local small-scale features in the bathymetry. This is apparent in the deep POLYMODE measurements along the Mid-Atlantic Ridge (Fu *et al.*, 1982). Spatial coherence from mooring to mooring at the POLYMODE sites was unique to the 1000 m flow field. At 4000 m, the mean currents followed local features in the bathymetry with scales smaller than the mooring separation. Features on these scales have been smoothed out of the model topography so that, at best, the model predicts a spatially averaged version of the currents. Perhaps the best evidence of the large-scale flows near the bottom comes from tracer distributions.

Dickson *et al.* (1985) analyzed 131 current-meter records of 6 to 24-month duration east of the Mid-Atlantic Ridge, from 19N to 54N. Many of the near-bottom flows were weak and statistically indeterminate. However, their conclusions confirm the overall nature of flows predicted in this study. In regions with reliable estimates (37N to 54N) they find cyclonic flow along topography with generally southward flow

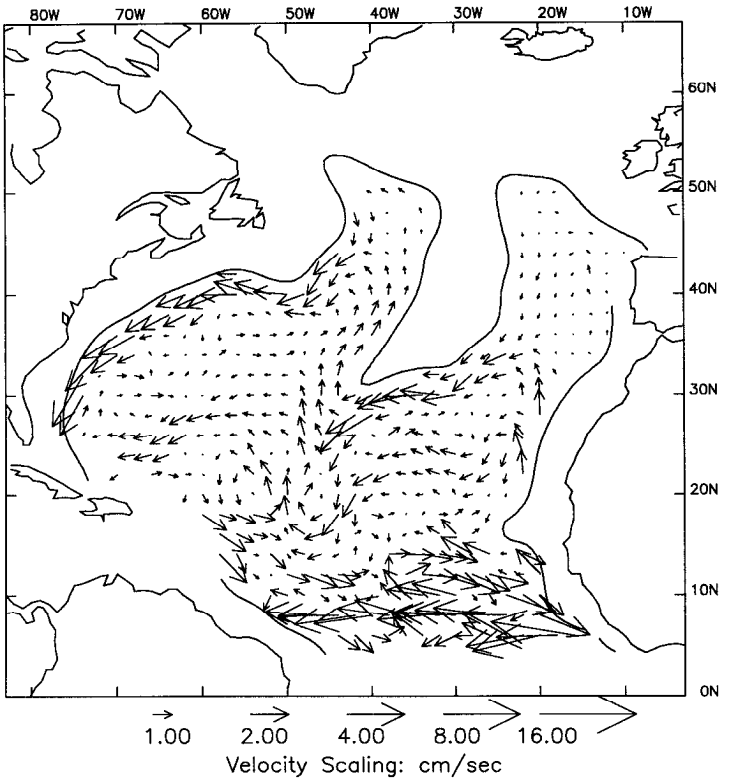

Figure 25. **u** at 3500 m for minimum-mixing solution in Experiment #2 in Section 5. Also plotted is 3500 m isobath. Vector scaling as in Figure 6.

along the ridge and a deep northward current along the eastern continental slope. Farther south the measurements are relatively sparse and they find only three directionally stable records. These records are near the bottom along 23W, at 30N and 35N, and indicate bottom-intensified poleward flow, not unlike that seen in Figure 26.

Lee and Ellett (1965) find evidence of equatorward flow along the eastern flank of the Mid-Atlantic Ridge in tracer distributions. They identify a water mass of northern origin at 2500–3500 m depth that underlies Labrador Sea Water in the eastern basin. They trace maxima in salinity and dissolved oxygen to show that the primary path of this flow in the eastern North Atlantic is along the eastern flank of the ridge. They found evidence of this water mass at their southernmost hydrographic section at 43N. Tsuchiya *et al.* (1991) show the same water mass extending to 41N and attribute its loss of distinctive characteristics to mixing with overlying high salinity water from the Mediterranean salt tongue.

The predicted 3500 m flow (Fig. 25) continues southward along the eastern flank of the ridge and turns westward into the western basin, crossing the ridge south of

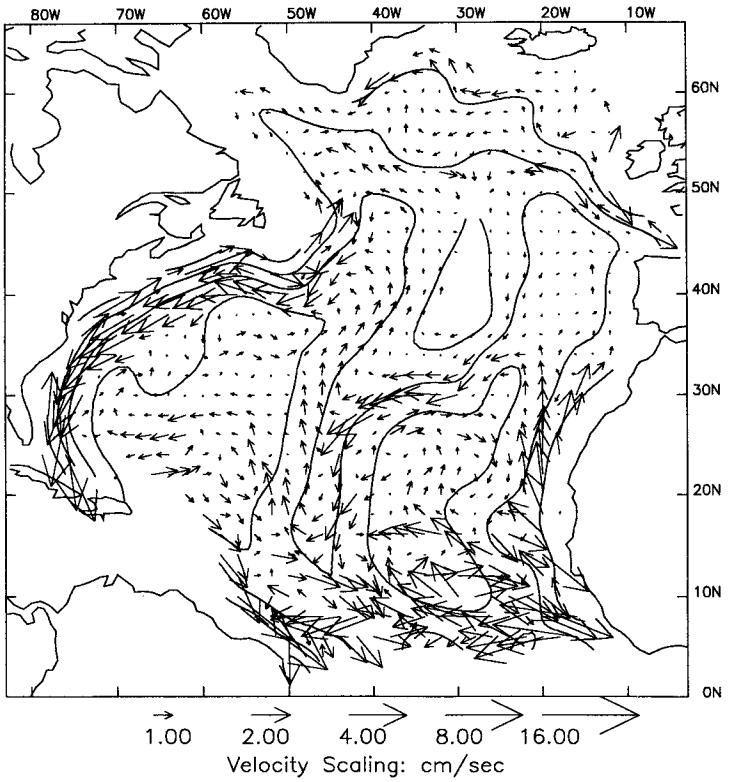

Figure 26. $\mathbf{u}_b$ for minimum-mixing solution in Experiment #2 in Section 5. Vectors are superposed on bathymetry plotted with contour interval of 1 km. Scaling as in Figure 6.

30N. The 3250 m oxygen distribution (Fukumori *et al.*, 1991) shows the broad oxygen minimum in the eastern basin extending westward across the ridge in the same latitude range. West of the ridge, the oxygen minimum extends westward into the basin and poleward along the ridge, a pattern which is qualitatively consistent with the predicted currents in Figure 25.

g. Deep flow in the northern North Atlantic. There is qualitative consensus among a variety of tracer-based studies about the deep water circulation in the northern North Atlantic (e.g. Ivers, 1975; Worthington, 1976). Dense water from the Norwegian-Greenland Sea flows over the shallow sills north of 60N to form the bottom waters of the northern basin. These waters are traced westward along the bottom topography into the Laboratory sea. It is thought that much of the flow diverts southward along the eastern flank of the Reykjanes Ridge (the northernmost branch of the Mid-Atlantic Ridge), with much of the flow passing west through the Gibbs Fracture Zone near 53N, 30W and then returning northward along the western flank of the Reykjanes Ridge. The predicted bottom currents flow in the same general

sense, from east to west along isobaths. There could be little evidence how the flow diverts around the Reykjanes Ridge because the ridge has been heavily smoothed in the bottom topography used here. Most of the predicted flow lies north of 55N.

It is generally thought that these bottom waters continue west along the slope, through the Labrador Sea, and become part of the deep western boundary current (e.g. Warren, 1981). This continuation is not apparent in the predictions, probably due to inadequate resolution of the bottom topography and hydrography at the edge of the computational domain. Few of the northernmost f/h contours extend into the Labrador Sea (Fig. 1).

h. Deep flow in the western basin. The classical deep western boundary current, the most prominent feature of the predicted bottom flow west of the ridge, is repeatedly observed in current measurements. Hogg (1983) presents a compilation of near-bottom current-meter measurements for the western basin, north of 30N and west of 45W. Time-averaged equatorward flows of up to 10 cm/sec are observed along the continental slope in water depths from 2000 m to 5000 m. Flows in excess of 10 cm/sec are found near 30N and farther to the south (Rosenfeld *et al.*, 1989; and Lee *et al.*, 1990). Flows of this sort are a prominent feature of the calculation (Fig. 26).

Hogg (1983) attempts to construct a large-scale bottom flow scheme from the available measurements. He suggests a multiple-cell pattern for the horizontal flow north of 35N. The largest cell of the pattern, north of 36N, is a cyclonic recirculation pattern with eastward flow from 45W to 65W and westward flow from 38N up to the continental slope. The predicted bottom flows are consistent with this large-scale circulation scheme. A second cell proposed by Hogg is based on small-latitudinal-scale flows near 36N, 55W. (These were discussed above in regard to the mid-depth measurements of Schmitz, 1980.) Predicted flows do not include this small-scale feature.

Based on the property distributions, the equatorward deep western boundary current has long been thought to continue south of 20N and across the equator (e.g. Wüst, 1935). In the model, there is equatorward flow along the continental slope of South America at least to 10N, but is not clear whether this flow is a continuation of the boundary flow farther to the north. This may be due to the unresolved shoaling of the bottom near the Caribbean.

Based on property distributions, the bottom water in the western basin of the North Atlantic has been determined to originate near the Antarctic (e.g. Wüst, 1935; Warren 1981). Antarctic bottom water can be traced northward along the continental slope of South America and across the equator west of the ridge. Between 8N and 16N, the western-boundary current is transposed into a northward-flowing eastern-boundary current along the western flank of the ridge (e.g. Warren, 1981). Some of this water crosses the ridge into the eastern basin of the North Atlantic through the

Vema Fracture Zone at 11N (McCartney *et al.*, 1991) with much of the bottom water spreading northward into the basin west of the ridge (Mantyla and Reid, 1983).

Many of the predicted bottom-flow features south of 15N are not robust, particularly near the eastern boundary. There is some indication of eastward flow across 11N and poleward flow in the deepest sections of the eastern basin, as suggested by McCartney *et al.* (1991). However there is no indication of poleward flow along the western flank of the Mid-Atlantic Ridge south of 12N.

Farther north along the western flank of the ridge, properties of the Antarctic bottom water can be traced northward into the deepest waters of the western basin (Mantyla and Reid, 1983). They are also found as far north as the Grand Banks of Newfoundland near 50N. North of 50N, properties along the bottom are characteristic of water of northern origin, indicating mixture of the two water masses near the Grand Banks.

The predicted bottom currents are consistent with these property distributions. Robust features in the calculcation include northward flow along the western flank of the ridge as far north as 50N, and northwestward flow into the deepest portions of the western basin south of 30N. At the latitude of the Grand Banks, the predicted currents along the ridge turn east along the bathymetry to merge with equatorward flow along the western boundary. This is where the observations of Mantyla and Reid (1983) indicate an admixture of the waters of northern and southern origin.

7. Comparison with previous studies

Mid-depth flow speeds predicted here are as much as an order of magnitude larger than those predicted in beta-spiral calculations (e.g. Stommel and Schott, 1977; Olbers *et al.*, 1985). The beta-spiral model uses geostrophic dynamics with prescribed ρ and eliminates velocity indeterminacy with a criterion that minimizes flow across density surfaces. Olbers *et al.* (1985) implemented the beta-spiral model using the same ρ field as here but with a different tracer-conservation criterion than that used by Stommel and Schott (1977). The beta-spiral models predict relatively weak $O(1$ mm/sec) mid-depth flows with no large-scale pattern. Two important differences between the beta-spiral model and the model used here could account for the discrepancy. First, beta-spiral models do not use top or bottom boundary conditions on the flow. Consequently, the dynamics are ignorant of bathymetry and the dynamically indeterminate velocity is an arbitrary scalar function of horizontal positon **x**. Second, the beta-spiral estimates are local in **x** (i.e. the practical velocity indeterminancy corresponds to an arbitrary *vector* function of **x**) so that the resulting velocity field is divergent. The reduced dynamical determinancy increases reliance on the tracer-conservation constraint for determining velocity. The small predicted velocities may be related to the fact that zero flow conserves any tracer in the absence of mixing and sources.

Hogg (1987) and Fukumori (1991) use geostrophic dynamics with prescribed ρ, but

they improve on the beta-spiral method by enforcing volumetric mass conservation over the entire model domain. Consequently, in these models the dynamical indeterminancy in velocity corresponds to an arbitrary *scalar* function of **x**. Hogg and Fukumori each consider the flow in rectangular areas (up to 20° on a side) in the vicinity of the Mediterranean salt tongue. The patterns of their predicted mid-depth flows have larger scales than the flows predicted by Olbers *et al.* (1985). Fukumori predicts weak 1200 m flow around the salt tongue consistent with Reid (1978), however, Hogg (1987) predicts westward flow at 1200 m in the same region. Although cross-isopycnal velocities in Hogg's solutions are comparable in magnitude to the 1000 m w's obtained in Section 5, his westward flow is an order of magnitude smaller, nearly equivalent to $\mathbf{u} = 0$ at 1000 m. As in the beta-spiral method, the dynamics used by Hogg and Fukumori are ignorant of the ocean bottom. Differences between their predictions may be attributable to differences in the tracer-conservation criteria.

Wunsch and Grant (1982) modeled the North Atlantic circulation using the section method, developed by Wunsch (1978), which uses essentially the same dynamics and boundary conditions as in this study. However, the flows predicted by Wunsch and Grant differ substantially from the flows predicted here. An important difference between the section method and our approach concerns the manner in which the dynamics are combined with data. In the section method, dynamical constraints are imposed along the perimeter of large horizontal domains. Since the data fields are not interpolated within the domains, free-mode variations are not constrained by f/h and the hyperbolic structure of the dynamics is lost. In the hyperbolic problem, the velocity indeterminancy at all points on the same f/h contour is eliminated by specifying velocity at only one of the points. In the section method, however, even though two points along the perimeter of the model domain may lie on the same f/h contour, the dynamically indeterminate velocity component at each point can be specified independently. In this sense, the dynamical uncertainty of the section method is much larger than it would be if the fields were interpolated in three dimensions. Also, the section method uses unsmoothed ρ and h data and allows dynamical misfit to compensate for sampling errors.

Provost and Salmon (1986) develop a methodology that also uses the same dynamics as here. As with the section method, Provost and Salmon use unsmoothed ρ and fairly well-resolved h. In contrast to the section method, the fields modeled by Provost and Salmon (1986) are spatially continuous. However, to compensate for data errors, their method allows dynamical misfit and incorporates a smoothness constraint that leads to an elliptic problem for the pressure. It remains unclear from their results whether the dynamical misfit is necessary for a reasonable circulation.

A large number of studies have combined prescribed ρ with numerical models having nonlinear dynamics and flux-gradient parameterizations for Reynolds stresses and property fluxes. Comparison with these studies is problematic because of the variety of built-in assumptions about the dynamics of unresolved scales. For example,

Sarmiento and Bryan (1982) prescribe ρ in a primitive-equation model. They find that unreasonably large vertical velocities dominate their solutions when smoothed ρ is incorporated directly into the model. They allow for data errors by admitting heat and fresh-water sources in their equations for temperature and salt conservation but only obtain "acceptable" model flows with unacceptably large internal source terms. They attribute this to the failure of their model to resolve mesoscale-eddy variability. However, to the extent that the mid-ocean velocity in their model satisfies nearly the same dynamics as in this study, it is possible that their use of ρ and h optimized as in Section 5 would ameliorate these problems.

8. Summary/discussion

The hyperbolic dynamics used in this study represent little more than the combined constraints of geostrophy, continuity and bottom topography. The validity of these dynamics in a local balance has been demonstrated with velocity measurements by Bryden (1980), Koblinsky *et al.* (1989) and others. Their results show that the non-locally forced deep flow along f/h contours, the component we refer to as the "dynamical free mode," often dominates the locally wind-forced flow across f/h contours. We enforce the hyperbolic dynamics in a global sense, over the entire North Atlantic. This accentuates the importance of the free-mode as an element of the large-scale flow. We estimate the magnitude of the free-mode component from its implications for the potential-density distribution.

Free-mode selection according to the classical condition of no net mass flux normal to the eastern boundary, the "ψ(east) = 0 condition," leads to unrealistic front-like features in the mid-ocean. This is seen in a calculation by Mellor *et al.* (1982), their Figure 11, and in our Figure 4 which reproduces many of the same features. There, front-like features exhibit vertical velocities that are implausibly large because they require correspondingly large cross-isopycnal flows. Front-like features no longer dominate the mid-ocean flow when the ψ(east) = 0 constraint is relaxed and free-mode selection is based instead on the minimum-mixing criterion. We do not conclude from these results that there must be net transport normal to the eastern boundary. On the contrary, f/h contours do not intersect the eastern boundary with realistic bathymetry, so free-mode selection has no direct bearing on mass transport normal to the coast. The reason the ψ(east) = 0 condition determines the free-mode here, and in earlier studies, is because of an ad-hoc decision to truncate the numerical grid somewhere offshore.

Near northwest Africa, from 15N to 30N, predicted flow follows f/h contours, parallel to the coast. This poleward flow is problematic as it requires large mass flux through the oxygen-minimum region that has been argued to be relatively quiescent (e.g. Luyten *et al.*, 1983). This strong flow prediction is sensitive to free-mode variations. This feature is also sensitive to density adjustment, as can be seen by comparing Figure 17 from Experiment 3 with Figure 7 for the unadjusted density

field. This is not suprising because, as pointed out in Section 2c, data errors are likely to have greater impact on predictions near lateral boundaries, where bottom-topography gradients are largest. We have little confidence, therefore, in predictions near the coast.

Away from the coasts, density adjustments have relatively little impact on the large-scale features in the horizontal flow. Their primary effect is to eliminate the remaining front-like features and anomalously large w's in the minimum-mixing solution without adjustments (Section 4). While wind-stress plays a role in the calculation, the dynamical impact of density adjustments exceeds the influence of plausible errors in the wind-stress measurements. Our ability to diagnose the circulation relies critically, therefore, on accurate knowledge of the density field, particularly in relation the large-scale bathymetry. Dynamically ignorant averaging of density and bottom topography apparently leads to front-like features. The density adjustments compensate for this, yielding dynamically compatible data.

This study leaves open questions relating to more highly resolved bathymetry. Koblinksy *et al.* (1989) showed that low-frequency currents respond to topography with O(100 km) length scales. If the large-scale flow "feels" bathymetry on a smaller scale than we have used, then our neglect of these scales amounts to a neglect of the potentially important "Reynolds-type" bottom stresses. The objective here has been to investigate the limit in which such terms are negligible, although this limit is only a hypothesis. Resolving bottom topography on smaller scales changes the nature of the hyperbolic problem by introducing multiple regions of closed f/h contours, or "shadow domes." Welander (1969) and Straub and Rhines (1990) discuss the existence of front-like features in association with such regions. They predict large currents flowing along the f/h contours that diverge, and then reconverge, around shadow domes. Flows of this type appear here in relation to the shadow dome at 30W, 40N. Results show them to be sensitive to free-mode selection and density errors. Whether these features are an inherent part of the large-scale circulation or an artifact of neglected scales remains unclear.

Robust aspects of the calculation include the strong O(1 cm/sec) mid-depth westward flow along the Mediterranean salt tongue, and the tendency for bottom currents to flow isobaths with shallow water to the right. Significant departure from these predictions requires unreasonably large cross-isopycnal flows. Nevertheless, the prediction of flow through the salt tongue implies that mixing must be important in maintaining this feature. Otherwise, currents must flow parallel to salinity isolines, as proposed by Reid (1978) and Fukumori (1991).

Although we use a minimum-mixing criterion to obtain reasonable results, the results do not imply that cross-isopycnal mixing is negligible. We use residual mixing in (2), and the second vertical derivative of potential density referenced to 1000 m, to compute cross-isopycnal diffusion coefficients. At mid-latitudes, the second derivative is everywhere negative and of order 10^{-3} gm/cm^3 km^2, thus upward velocities

correspond to positive diffusivities. The diffusivities are of order 1 cm^2/sec and vary in $\mathbf{x}$ on the same scales as w. The amplitudes, though large, compare with values that Hogg (1987) computed for a region in the salt tongue.

Whereas the minimum-mixing criterion is admittedly ad hoc, we use it only as a weak constraint. Consequently, the results are not sensitive to details of the criterion. The penalty for cross-isopycnal flow serves merely to bound the w with a plausible range of magnitudes. Any approximately conserved tracer that defines a material surface with slopes that are comparable to isopycnal slopes will serve the same purpose. Also, because of the simple vertical structure in the subthermocline velocity field ($w/|\mathbf{u}|$ varies nearly linearly in z with maximum amplitude at the bottom), the solutions are not sensitive to the depth at which the criterion is applied. We found similar results (not presented), for example, when we employed a criterion that minimized mean-square w_b.

Acknowledgments. This work was supported by the National Science Foundation (OCE-8901720) and the Office of Naval Research (ONR-N00014-89-J-1046). We thank John C. Marshall and anonymous reviewers for their stimulating comments on the final manuscript.

REFERENCES

Arhan, M., A. C. De Verdiere and H. Mercier. 1989. Direct observations of the mean circulation at 48N in the Atlantic Ocean. J. Phys. Oceanogr., *19,* 161–181.

Bogden, P. S. 1991. The North Atlantic Circulation: Combining Simplified Dynamics with Hydrographic Data. Ph.D. Thesis, Unversity of California at San Diego, 102 pp.

Bryden, H. L. 1980. Geostrophic vorticity balance in midocean. J. Geophys. Res., *85,* 2825–2828.

Dickson, R. R., W. J. Gould, T. J. Müller and C. Maillard. 1985. Estimates of the mean circulation in the deep (> 2000 m) layer of the eastern North Atlantic. Prog. Oceanogr., *14,* 103–127.

Fu, L.-L., T. Keffer, P. P. Niiler and C. Wunsch. 1982. Observations of mesoscale variability in the western North Atlantic: A comparative study. J. Mar. Res., *40,* 809–848.

Fukumori, I. 1991. Circulation about the Mediterranean tongue: an analysis of an EOF-based model ocean. Prog. Oceanogr., *27,* 197–224.

Fukumori, I., F. Martel and C. Wunsch. 1991. The hydrography of the North Atlantic in the early 1980s. An Atlas. Prog. Oceanogr., *27,* 1–110.

Gould, W. J. 1983. The Northeast Atlantic Ocean, *in* Eddies in Marine Science, A. R. Robinson ed., Springer-Verlag, Berlin, 145–157.

Hellerman, S. and M. Rosenstein. 1983. Normal monthly wind stress over the world ocean with error estimates. J Phys. Oceanogr., *13,* 1093–1104.

Hogg, N. G. 1983. A note on the deep circulation of the western North Atlantic: its nature and causes. Deep-Sea Res., *30,* 945–961.

—— 1987. A least-squares fit of the advective-diffusive equations to Levitus Atlas data. J. Mar. Res., *45,* 347–375.

Ivers, W. E. 1975. The deep circulation in the northern North Atlantic, with especial reference to the Labrador Sea. Ph.D. Thesis, University of California at San Diego, 179 pp.

Koblinsky, C. J., P. P. Niiler and W. J. Schmitz, Jr. 1989. Observations of wind-forced deep ocean currents in the North Pacific. J. Geophys. Res., *94,* 10773–10790.

Krauss, W. 1986. The North Atlantic Current. J. Geophys. Res., *91,* 5061–5074.

Lee, A. and D. Ellett. 1965. On the contribution of overflow water from the Norwegian Sea to the hydrographic structure of the North Atlantic Ocean. Deep-Sea Res., *12,* 129–142.

Lee, T. N., W. Johns, F. Schott and R. Zantopp. 1990. Western boundary current structure and variability east of Abaco, Bahamas at 26.5N. J. Phys. Oceanogr., *20,* 446–466.

Leetmaa, A., P. Niiler, and H. Stommel. 1977. Does the Sverdrup relation account for the Mid-Atlantic circulation? J. Mar. Res., *35,* 1–10.

Levitus, S. 1982. Climatological atlas of the world ocean. NOAA Technical Paper 13, National Oceanic and Atmospheric Administration, Rockville, Maryland, 173 pp.

Luyten, R. J., J. Pedlosky and H. Stommel. 1983. The ventilated thermocline. J. Phys. Oceanogr., *13,* 292–309.

Mantyla, A. W. and J. L. Reid. 1983. Abyssal characteristics of the World Ocean waters. Deep-Sea Res., *30,* 805–833.

Mellor, G. L., C. R. Mechoso and E. Keto. 1982. A diagnostic calculation of the general circulation of the Atlantic Ocean. Deep-Sea Res., *29,* 1171–1192.

McCartney M. S., S. L. Bennett and M. E. Woodgate-Jones. 1991. Eastward flow through the Mid-Atlantic Ridge at 11N and its influence on the abyss of the eastern basin. J. Phys. Oceanogr., *21,* 1089–1121.

McWilliams, J. C., E. D. Brown, H. L. Bryden, C. C. Ebbesmyer, B. A. Elliott, R. H. Heinmiller, B. Lien Hua, K. D. Leaman, E. J. Lindstrom, J. R. Luyten, S. E. McDowell, W. B. Owens, H. Perkins, J. F. Price, L. Regier, S. C. Riser, H. T. Rossby, T. B. Sanford, C. Y. Shen, B. A. Taft and J. C. Van Leer. 1983. The local dynamics of eddies in the western North Atlantic, *in* Eddies in Marine Science, A. R. Robinson, ed., Springer-Verlag, Berlin, 92–113.

Olbers, D. J., M. Wenzel and J. Willebrand. 1985. The inference of North Atlantic circulation patterns from climatological hydrographic data. Rev. Geophys. Space Phys., *21,* 313–356.

Owens, W. B. 1991. A statistical description of the mean circulation and eddy variability in the northwestern Atlantic using SOFAR floats. Prog. Oceanogr., *28,* 257–303.

Owens, W. B., J. R. Luyten and H. L. Bryden. 1982. Moored velocity measurements on the edge of the Gulf-Stream recirculation. J. Mar. Res., *40,* (Suppl.) 509–524.

Owens. W. B., P. L. Richardson, W. J. Schmitz, Jr., H. T. Rossby and D. C. Webb. 1988. Nine-year trajectory of a SOFAR float in the southwestern North Atlantic. Deep-Sea Res., *12,* 1851–1857.

Pedlosky, J. 1979. Geophysical Fluid Dynamics. Springer-Verlag, New York, 624 pp.

Pingree, R. D. 1973. A component of Labrador Sea water in the Bay of Biscay. Limno. Oceanogr., *18,* 711–718.

Provost, C. and R. Salmon. 1986. A variational method for inverting hydrographic data. J. Mar. Res., *44,* 1–34.

Reid, J. L. 1978. On the middepth circulation and salinity field in the North Atlantic Ocean. J. Geophys. Res., *83,* 5063–5067.

—— 1979. On the contribution of Mediterranean Sea outflow to the Norwegian-Greenland Sea. Deep-Sea Res., *26,* 1199–1223.

Riser, S. C., H. Freeland and H. T. Rossby. 1978. Mesoscale motions near the deep western boundary of the North Atlantic. Deep-Sea Res., *25,* 1179–1191.

Rosenfeld, L. K., R. L. Molinari and K. D. Leaman. 1989. Observed and modeled annual cycle of transport in the Straits of Florida and east of Abaco Island, the Bahamas (26.5N). J Geophys. Res., *94,* 1199–1223.

Rossby, H. T., S. C. Riser and A. J. Mariano. 1983. The western North Atlantic—a lagrangian viewpoint, *in* Eddies in Marine Science, A. R. Robinson, ed., Springer-Verlag, Berlin, 66–91.

Sarmiento, J. L. and K. Bryan. 1982. An ocean transport model for the North Atlantic. J. Geophys. Res., *87,* 394–408.

Schmitz, W. J., Jr. 1980. Weakly depth-dependent segments of the North Atlantic circulation. J. Mar. Res., *38,* 111–133.

—— 1984. Abyssal eddy kinetic energy in the North Atlantic. J. Mar. Res., *42,* 509–536.

Schmitz, W. J., Jr., J. F. Price and P. L. Richardson. 1988. Recent moored current meter and SOFAR float observations in the eastern Atlantic near 32N. J. Mar. Res., *46,* 301–319.

Stommel, H. and F. Schott. 1977. The beta spiral and the determination of the absolute velocity field from hydrographic station data. Deep-Sea Res., *29,* 325–329.

Straub, D. N. and P. B. Rhines. 1990. Effects of large-scale topography on abyssal circulation. J. Mar. Res., *48,* 223–253.

Sverdrup, H. U. 1947. Wind-driven currents in a baroclinic ocean; with application to the equatorial currents of the eastern Pacific. Proc. Nat. Acad. Sci., USA, *33,* 318–326.

Sverdrup, H. U., M. W. Johnson and R. H. Fleming. 1942. The Oceans: Their Physics, Chemistry and General Biology. Prentice-Hall, Engelwood Cliffs, New Jersey, 1087 pp.

Talley, L. D. and M. S. McCartney. 1982. Distribution and circulation of Labrador Sea water. J. Phys. Oceanogr., *12,* 1189–1205.

Tsuchiya, M. 1985. Evidence of a double-cell subtropical gyre in the South Atlantic Ocean. J. Mar. Res., *43,* 57–65.

Tsuchiya, M., L. D. Talley and M. S. McCartney. 1992. An eastern Atlantic section from Iceland southward across the equator. Deep-Sea Res., *39,* 1885–1917.

Warren, B. A. 1981. Deep circulation of the World Ocean, *in* Evolution of Physical Oceanography, B. Warren and C. Wunsch, eds., MIT Press, 6–41.

Welander, P. 1969. Effects of planetary topography on deep-sea circulation. Deep-Sea Res., *16*(Suppl), 369–392.

Worthington, L. V. 1976. On the North Atlantic Circulation. The Johns Hopkins Oceanographic Studies, *6,* 110 pp.

Wunsch, C. 1978. The North Atlantic general circulation west of 50W determined by inverse methods. Rev. of Geophys. Space Phys., *16,* 583–620.

Wunsch, C. and B. Grant. 1982. Towards the general circulation of the North Atlantic ocean. Prog. in Oceanogr., *11,* 1–59.

Wüst, G. 1935. Schichtung und Zirkulation des Atlantischen Ozeans. Die Stratosphare, *in* Wissenschaftliche Ergebnisse der Deutschen Atlantischen Expedition auf dem Forschungs- und Vermessungsschiff "Meteor" 1925–1927, *6:* Part 1, 2, 180 pp.

Zenk, W. and T. J. Müller. 1988. Seven-year current meter record in the eastern North Atlantic. Deep-Sea Res., *35,* 1259–1268.

Received: *20 May, 1992;* revised: *12 January, 1993.*